CONDITIONING OF PLATINUM NANOPARTICLE CATALYSTS FOR IMPROVED HYDROGEN GENERATION ON P3HT:PCBM BULK HETEROJUNCTION PHOTOCATHODES

by

Reynolds James Ivins II

A thesis submitted to the faculty of
The University of North Carolina at Charlotte
in partial fulfillment of the requirements
for the degree of Master of Science in
Chemistry

Charlotte

2015

Approved by:

_____
Dr. Michael Walter

_____
Dr. Bernadette Donovan-Merkert

_____
Dr. Jordan Poler

_____
Dr. HaiTao Zhang

ABSTRACT

REYNOLDS JAMES IVINS II. Conditioning of platinum nanoparticle catalysts for improved solar hydrogen generation on a P3HT:PCBM bulk heterojunction photocathode. (Under the direction of DR. MICAHEL GEORGE WALTER)

This work aims to design, develop, and investigate the capacity of a metal catalyst-coated organic photoelectrode to produce molecular hydrogen when illuminated in acidic media. 3-5 nm platinum nanoparticles (PtNPs) were synthesized, treated to remove bound surface ligands and subsequently found to function as improved catalysts for the hydrogen evolution reaction (HER). Thermal processing of the catalyst was the most successful removal method. The exchange current density decreased only slightly while the Tafel slope decreased considerably from 74.1 ± 1.0 mV dec^{-1} to 41.5 ± 1.1 mV dec^{-1} following heat treatment at 200 ^{o}C. The low Tafel slope indicates that catalysis on the NP surface proceeds by a Vollmer-Heyrovsky Mechanism. An attempt was made to utilize the characterized PtNPs as embedded electrocatalysts on a bulk heterojunction (BHJ) blend of poly(3-hexylthiophene): [6,6]-phenyl C_{61}-butyric acid methyl ester (P3HT:PCBM). In solution, the bare (no catalyst) BHJ photoelectrode showed good light response, achieving an open circuit voltage of 414 mV and short-circuit current density of 0.013 mA cm^{-2}, resulting in an overall solar-to-hydrogen efficiency of 0.016%. However, the catalyst-sensitized BHJ appeared to function only as a dark catalyst, demonstrating almost no response to light. While further investigations are needed, we believe steps must ultimately be taken to prevent direct touching of the platinum nanoparticle layer with the organic film while maintaining electrical contact across the semiconductor, catalyst, and solution interfaces.

ACKNOWLEDGMENTS

I take this opportunity to show gratitude for those who have given me the means to complete this work and contributed to my growth as a scientist. I wish to first express sincere thanks to my advisor, Dr. Michael G. Walter for his indispensable guidance over the years. His expertise with molecular semiconductors has been vital to this project and he has always been available to give advice, direction, or muse about the day-to-day. My thesis committee also deserves my heartfelt appreciation for their contributions to this research. Dr. Bernadette Donovan-Merkert has shared her electrochemistry knowledge and always been supportive during my time in this program. Dr. Jordan Poler has been crucial to the experimental design process and a source for motivation, giving me the push we have all needed at times. Lastly, Dr. HaiTao Zhang has provided a valued perspective from his background in materials science and engineering.

I would also like to thank several members of the Walter Research Group. Nick Grubich, Li Nguyen, Graham Collier, and the current WRG have been a pleasure to work alongside over the years. Dr. Angy Ortiz deserves special recognition as my potentiostat guru. I owe gratitude to Drew Tobias of the Marcus Jones Research Group for his assistance with the Transmission Electron Microscope and for always being available to unwind and reflect on our graduate research. I am also grateful to those who have directly contributed to this work. Undergraduate students Vrushab Gowda and Igor Oliveira Tavares have both offered large portions of their time and have been dedicated lab associates. Finally, thanks must be given to Caroline Kennedy and Robin Burns. They are central to the chemistry department and true sorcerers of administration magic. I am glad to have known all of those mentioned as colleges and friends.

TABLE OF CONTENTS

LIST OF ABBREVIATIONS

AM 1.5	air mass 1.5
BHJ	bulk heterojunction
CV	cyclic voltammetry
e^-	electron
E_g	band gap energy
ECSA	electrochemically active surface area
EDX	energy dispersive X-ray spectroscopy
EtOH	ethanol
h^+	electron hole
HER	hydrogen evolution reaction
HOAc	acetic acid
HOMO	highest occupied molecular orbital
IEA	International Energy Agency
IR	infrared spectroscopy
ITO	indium tin oxide
J_{sc}	short circuit current density
LSV	linear sweep voltammetry
LUMO	lowest unoccupied molecular orbital
NP	nanoparticle
OER	oxygen evolution reaction
OFET	organic field effect transistor
OPV	organic photovoltaic

P3HT	poly(3-hexylthiopene)
PCBM	[6,6]-phenyl C_{61}-butyric acid methyl ester
PEC	photoelectrochemical cell
PEDOT	poly(3,4-ethylenedioxythiophene)
PSA	projected surface area
PSS	poly(styrenesulfonate)
$Pt(acac)_2$	Platinum (II) acetylacetonate
PtNPs	platinum nanoparticles
PV	photovoltaic
SCE	saturated calomel electrode
SEM	scanning electron microscope
SHE	standard hydrogen electrode
SSA	substrate surface area
STH	solar-to-hydrogen efficiency
TEM	transmission electron microscope
TGA	thermogravimetric analysis
V_{oc}	open circuit potential

CHAPTER 1:INTRODUCTION

1.1 Significance: Alternative Energies

Declining fossil fuel availability and the detrimental effects of combustion products (CO_2 and other greenhouse gasses) are major issues facing today's energy economy. Together they are driving the world population to reconsider how we collect and use our energy sources. Amongst the renewable alternatives (solar, wind, hydroelectric, geothermal, etc.), adoption of a widespread solar-based energy infrastructure is perhaps the most viable. According to the International Energy Agency (IEA), oil, coal and natural gas accounted for approximately 65% of the total estimated world energy consumption of 104,426 TW-h in 2012.[1] In comparison, the theoretical potential of solar power reaching the planet's surface at a given moment has been calculated to be 89,300 TW.[2] Over a period of just six hours, enough attainable sunlight will strike earth's landmasses to supply mankind's energy needs for an entire year Harnessing even a fraction of this free energy will also have substantial long-term benefits to the environment through the reduction of greenhouse gas emissions. Furthermore, the IEA has proposed that a growing adoption of alternative energies can help strengthen national economies through the lessening of foreign fossil fuel dependence.

Photovoltaic (PV) devices successfully convert solar photons into usable electricity. Only certain materials will emit electrons under illumination of light with a

characteristic energy. Semiconductors are so-named because their valence and conduction band are separated by an appreciable gap (E_g). When struck by a sufficiently energetic photon ($E_{photon} > E_g$), an electron in the valence band will be excited to the conduction band where it can be harnessed to do work. The size of the band gap therefore determines the wavelength (energy) of light that the semiconductor will absorb. To design a PV device with the best performance, chosen semiconductors should have band gaps tailored to absorb the maximum portion of solar flux that reaches the earth. The solar spectrum (Figure 1) gives valuable information about the availability of solar photons that reach earth.

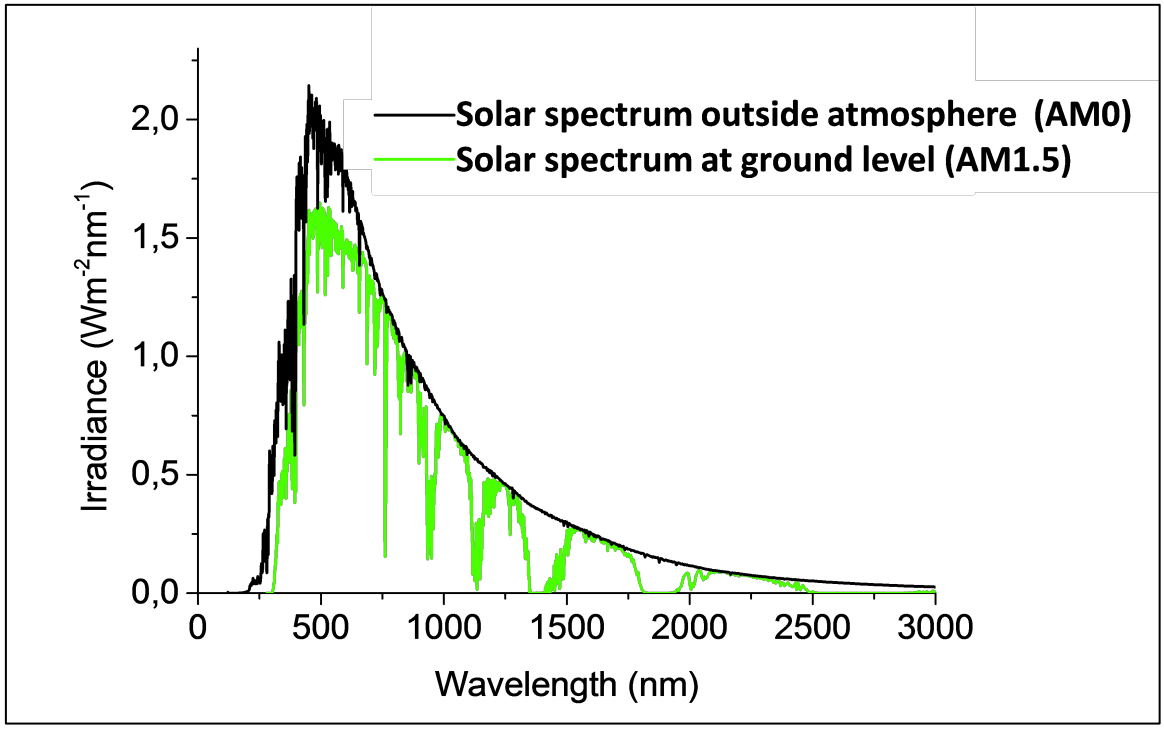

Figure 1: Incident solar radiation on the atmosphere (Air Mass 0) and planetary surface (Air Mass 1.5, standard testing condition).[3]

Ultraviolet light, although more energetic than visible light, is substantially filtered by the atmosphere and considerably less abundant on the planet's surface (AM 1.5) as a result. For this reason, the majority of solar cells to date are visible-light driven systems.

First generation PV technologies dominate the market and are based on inorganic semiconductors, primarily crystalline silicon. This generation is characterized by practical conversion efficiencies (15-20% for commercial Si wafers) and high stability. Despite an established infrastructure, silicon refinement is still highly energy intensive and production costs are high. Second generation PVs are composed of amorphous silicon and other inorganic semiconductors such as indium, germanium, gallium, cadmium, tellurium, selenium and others. By avoiding the use of high purity silicon wafers, these cells have a much lower production cost but are typically less efficient that the previous generation. However, because high vacuum and temperature treatments are still needed, energy consumption during device fabrication still limits widespread adoption.

While these generations may be presently sustainable, research and development of solar energy conversion technologies is being driven towards a third generation of inexpensive and easily processed materials. Lately, organic photovoltaics (OPVs) have become the subject of extensive study and have rapidly advanced to achieve commercial power conversion efficiencies around 5% with some recent reports exceeding 10%.[4,5] Such devices are economically competitive with earlier generations due to their extremely low production costs. OPVs integrate various semiconductive polymers, small dye molecules and even some inorganic components into structured architectures that

facilitate excitonic movement and charge dissociation (addressed in further detail in section 1.4). OPVs are surprisingly versatile devices. Organic synthesis affords an incredible amount of control over molecular structure, leading to a range of tunable properties such as molecular orbital energy levels and band gap, molecular and polymer weight, conjugation length, structural rigidity and wetting ability.[4] More impressively, device architectures can be designed and readily prepared in the laboratory via solution-deposition techniques that are much simpler than the vacuum-deposition methods used for conventional cell processing. This additionally cuts fabrication costs and allows OPV components to be printed on flexible plastic substrates in almost any conceivable pattern. While not yet as efficient as current generations, these plastic solar cells have a capacity for integration into building architectures and consumer products unlike any present technology.

1.2 Solar Fuels via Artificial Photosynthesis

Regardless of materials and device architecture, all solar technologies face the same fundamental challenge- any captured solar energy must eventually be stored or risk being lost. While a PV cell may work properly at midday, nighttime is problematic. Once the sun has set, energy production will cease but demand will not. To continue to use this clean energy source at night, it must be stockpiled in another form. In this way, fossil fuels have a practical advantage over solar power because they can be stored long term and transported over extreme distances. The development of solar fuel technologies aims to address this shortcoming by storing collected solar energy in the readily accessible form of a chemical bond.

Because photovoltaics transduce solar energy to electrical current, a solar battery is often the first storage medium considered. However, because batteries fundamentally rely on a chemical reaction (and by extent, chemical equilibrium), they are poor at releasing energy quickly and efficiently. The low power density of batteries is precisely why they are almost completely ignored when it comes to power-intensive applications. For this reason, fields such as transportation still exploit the burning of fossil fuels where an immense amount of energy is released quickly as hydrocarbon bonds are broken during the combustion process. To create a power-dense alternative to fossil fuels, the sun's energy must also be stored as chemical bond, thereby making a solar fuel. "Solar Hydrogen" therefore refers to the notion of storing energy harnessed from sunlight as the H-H bond.

Hydrogen is a clean burning, zero-emission alternative to current fossil fuels. When traditional hydrocarbons combust in the presence of oxygen, stoichiometric quantities of CO_2 and H_2O are produced. CO_2 is an undesirable product side product; CO_2 emissions build up in the earth's atmosphere, contributing to the greenhouse gas effect and global warming. On the other hand, the combustion of H_2 with oxygen yields only water, making it a carbon-neutral fuel.

The majority of present hydrogen supplies feed directly into chemical industries such as ammonia production, metal/glass industries, and others. However, there does exist a growing niche market and infrastructure for hydrogen as a chemical fuel. The National Aeronautic and Space Administration (NASA) uses liquid hydrogen as their rocket fuel of choice, not because it's environmentally friendly, but because it's extremely light.

Hydrogen is the most abundant element in the universe and the most energy dense (approximately 142 MJ kg^{-1}) fuel by mass.[6]

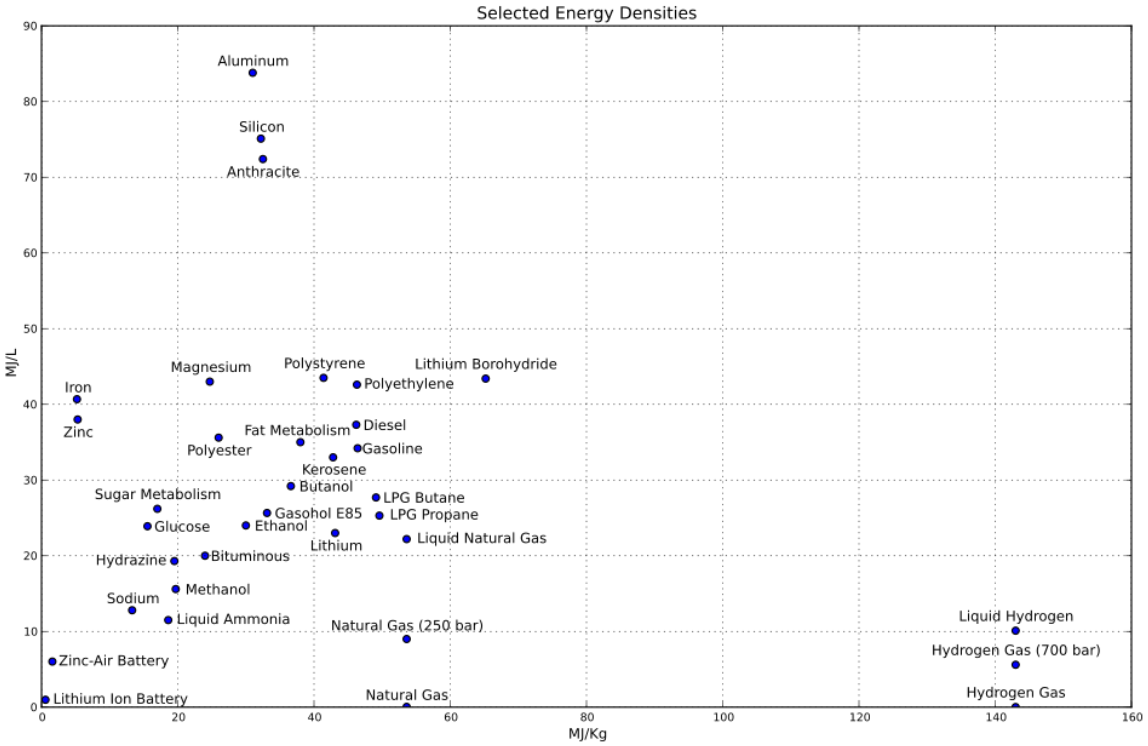

Figure 2: Selected energy densities. Public domain.

This means, pound for pound, hydrogen combustion is capable of producing more clean energy than natural gas (54 MJ kg^{-1}), gasoline (46 MJ kg^{-1}), and coal (32 MJ kg^{-1}). In terms of personal transportation, high efficiency hydrogen combustion engines do exist at present. For instance, BMW's Hydrogen 7 contains a dual combustion engine that can run on traditional gasoline or liquid hydrogen.[7]

Hydrogen can also be combined with molecular oxygen in a fuel cell, thereby converting its chemical energy back into electricity. Personal transport vehicles based on

fuel cells already exist and commercial transports such as the Boeing hydrogen-powered aircraft are also being pursued.[8]

While hydrogen is a carbon-neutral fuel, current industrial methods for its production certainly are not. Of the 40 megatons of hydrogen produced yearly, approximately 48% of the demand is generated directly from natural gas, 30% by the petroleum industry, and 18% from the gasification of coal.[9] In comparison, clean methods like water electrolysis account for the remaining 4%.[9] To date, the majority of commercial hydrogen is generated via the steam reforming of natural gas (methane). In the presence of a nickel catalyst at high temperatures (700-1100 ^{o}C) steam (H_2O) reacts with methane (CH_4) to produce stoichiometric amounts of carbon monoxide (CO) and hydrogen gas.[10] Even more hydrogen can be liberated by the water-gas shift reaction where the produced CO is reacted with more water vapor to produce CO_2 and H_2. Unfortunately, both of these processes involve the release of significant quantities of greenhouse gasses (CO and CO_2) and are quite energy intensive, contributing 52-68% of the final hydrogen cost of 1.2-3.5 US$ kg^{-1}.[10] Luckily, there is a clean source of accessible hydrogen all around us. Water contains two atoms of hydrogen per molecule and is ubiquitous across civilizations.

In an effort to generate this fuel through a clean pathway, H_2 gas can be produced by the sunlight-mediated electrolysis of water in a process colloquially referred to as artificial photosynthesis. As evidenced by the name, this process borrows heavily from solar conversion systems found in nature.

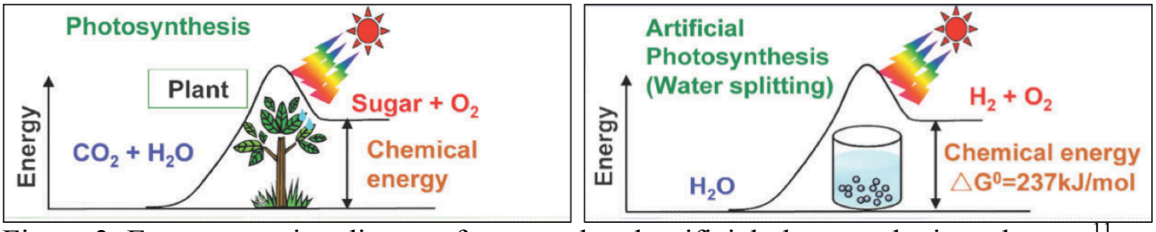

Figure 3: Energy-reaction diagram for natural and artificial photosynthetic pathways.[11]

Every night, plants face the same need for energy storage as the solar industry. Photosynthetic plants use the captured energy from sunlight to split (oxidize) water and reduce CO_2 molecules to make carbohydrates. At night, these simple sugars are metabolized as plant food. Similarly, artificial photosynthesis involves splitting water with the power of the sun. The goal is not sugar production, but the generation of hydrogen gas instead. Neither of these processes is trivial; both require the collaborative cohesion of many structures and mechanisms working in unity. To envision an artificial system capable of simultaneously driving water oxidation and hydrogen reduction, several central concepts must be understood.

1.3 Solar Water Splitting Cells

Hydrogen fuel, produced by the photocatalytic electrolysis of water, has demonstrated considerable value as a potential source of clean, renewable energy.[12,13] A system capable of efficiently splitting liquid water into its component elements under light irradiation is called a photoelectrochemical cell (PEC). Total water electrolysis consists of two redox half reactions: the oxygen evolution reaction (OER) and hydrogen evolution reaction (HER), as summarized in Figure 4.

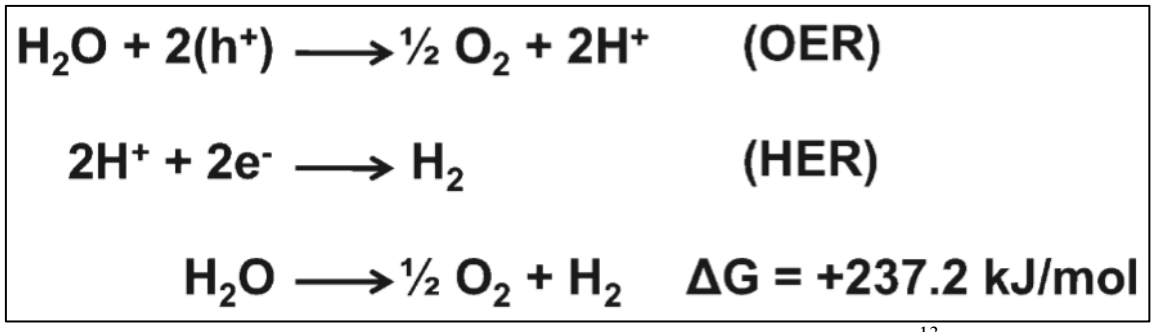

Figure 4: Thermodynamic requirement for water splitting half reactions[13]

The schematic above reveals the two redox reactions that constitute a water splitting cell. In a complete cell, water is first oxidized (split) at one electrode while protons are subsequently reduced to molecular hydrogen at the counter electrode. An efficient PEC system must be able to simultaneously drive each reaction, generating gaseous oxygen and hydrogen at the anode and cathode, respectively.

Figure 4 also reports the Gibbs free energy value (ΔG) for the overall electrolysis reaction. The Gibbs free energy value offers vital information on the spontaneity of a chemical reaction. The value for ΔG tells the direction and magnitude the reaction must shift to reach equilibrium. A positive ΔG means the reaction will not proceed spontaneously; energy must be put into the system to shift the equilibrium to the product side. This makes sense qualitatively, as the breakdown of water into its components is indisputably a nonspontaneous process.

In a similar manner to the Gibbs free energy relation, the potential of an electrochemical cell expresses how far a redox reaction is from equilibrium. The Nernst equation can then be used to describe the relationship between this cell potential and the standard state cell potential, as follows:

$$E_{cell} = E^0 - \frac{RT}{nF}\ln(Q) \quad (1)$$

where the E_{cell} refers to the cell potential (V) compared to the standard cell potential E^0. Q is the reaction quotient, R is the ideal gas law constant (R = 8.314 J K^{-1} mol^{-1}), T is the absolute temperature (K), F is the Faraday constant (F = 9.648x10^4 C^{-1} mol^{-1}), and n is the number of moles of electrons transferred in the redox reaction. By dividing both sides of the equation above by nF, the Nernst equation is transformed into equation (2).

$$nFE = NFE^0 - RTln(Q) \quad (2)$$

The Nernst equation can then be equated to Gibbs free energy (equation 3), giving ΔG in terms of E (equation 4).

$$\Delta G = \Delta G^0 + RTln(Q) \quad (3)$$

$$\Delta G = -nFE \quad (4)$$

The thermodynamic water splitting requirement can now be converted to the electrochemical potential needed to drive the electrolysis by moving two moles of electrons. Substituting our ΔG value (237.2 kJ mol^{-1}) into equation 4 above indicates that an energy of 1.23 eV is the thermodynamically required minimum potential to split water into its elemental components.

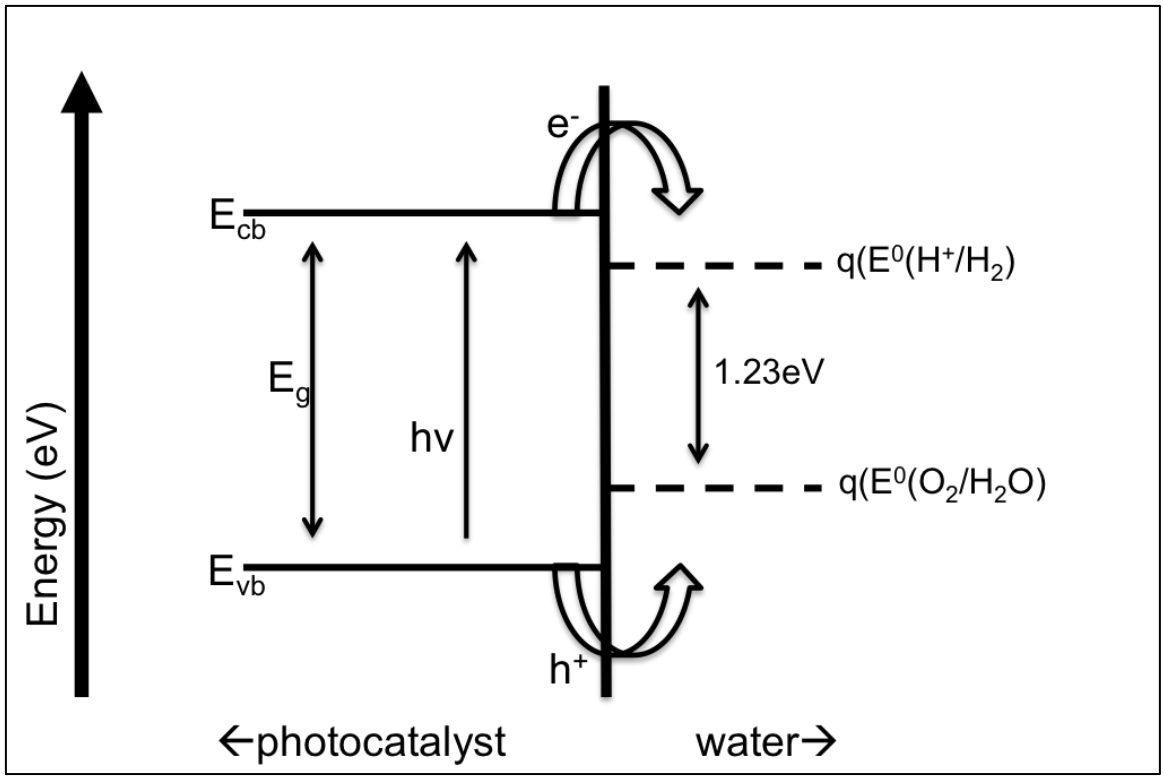

Figure 5: Band diagram for semiconductor/water interface.

As seen above, any photocatalyst with a sufficiently wide optical band gap ($E_g \geq 1.23$ eV) should therefore be able to drive the electrolysis of water under normal conditions. While a band gap of 1.23 eV is the minimum needed to split water, an overpotential (usually on the order of 1.7-1.8 eV) must be produced to compensate for the additional bias needed to drive the reaction at the semiconductor/liquid junction. To function with minimum losses, a complete PEC should combine some PV system (light harvester) and an electrolyzer (water splitter) in a single device.

To accomplish this, several material and energetic requirements must be considered for our system: I.) Photon absorption- the photoactive material must be engineered with sufficient band gap for water splitting. To drive water oxidation, band energy must be greater than 1.23 eV or 1008 nm. II.) Charge separation and transport-

recombination must be suppressed while free charge carriers (electrons and holes) are encouraged to migrate to opposite electrodes and drive corresponding half-reactions. III.) Surface catalysis- Finally, surface reaction sites, each with a specific electrocatalyst, must be constructed at both electrodes to promote each half reaction (water oxidation at the anode, proton reduction at the cathode). The use of heterogeneous catalysts conveniently traps electrons (HER) or holes (OER) and provide a lower energy barrier for these reactions.

In 1972, Honda and Fujishima first demonstrated water photolysis on the surface of a TiO_2 photoelectrode.[14] While a pioneering achievement, such a device was far from industrial-scale implementation. A wide band gap semiconductor like TiO_2, is sensitive to ultraviolet light, which despite being more energetic is much less available than visible light in the solar spectrum. Luckily, visible light has sufficient energy to split water and can penetrate the medium as well. Additionally, a commercially applicable photoelectrode should be environmentally friendly and resistant to corrosion. With the recent advent of third generation OPVs, the integration of green, semiconducting dyes and polymers into the manufacturing of cheap, flexible devices appears possible. As a result, there exists a desire to create and study visible light-driven (narrow band gap) photocatalytic systems based on solution-processable organic polymer semiconductor blends.

1.4 Organic Semiconductors in Bulk Heterojunction Architectures

The fact that polymers, previously considered only in terms of insulating plastics, could behave as semiconductors was a monumental discovery that earned Alan Heeger, Alan MacDiarmid and Hideki Shirakawa the 2000 Nobel Prize in Chemistry. Today,

conjugated polymers have been catapulted into a variety of electronics application and are the basis of light absorption in OPVs (and now organic PECs). Their semiconductive properties arise from the continuous, alternating network of single and double bonds that give rise to delocalized π states along the length of the polymer chain.

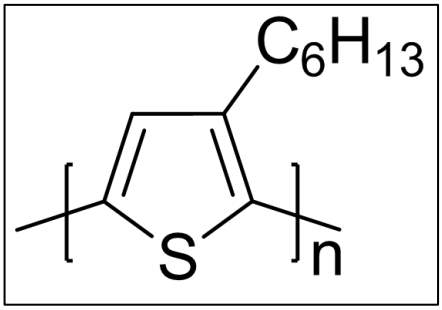

Figure 6: The conductive polymer P3HT.

To date, poly(3-hexylthiophene) (P3HT) is the most studied light absorbing polymer used OPVs, with typical device efficiencies of 4-5%.[15–18] Regioregular P3HT can be prepared through a variety of synthetic methods and is relatively inexpensive.[19] Reasons for P3HT's widespread use in OPVs and organic field effect transistors (OFETs) include good chemical stability, high hole mobility, and narrow optical band gap (1.7-1.9 eV).[20] The polymer's absorption spectrum is characterized by a broad absorption in the visible range (400-700 nm) of the electromagnetic spectrum as a result of its extended conjugation. Fully conjugated polymers like P3HT exhibit anisotropic structures with high conductivity due to π-π overlap between monomers along the chain's length. When present in the solid state (i.e. a photoactive film), a red shift in absorbance arises resulting from intermolecular arrangement of the six-carbon side chain away from the thiophene

backbone. Further enhancement in terms of intensity and red-light sensitivity can be obtained through thermal annealing of P3HT films which reorganizes molecular packing.

Fast and efficient charge transfer is just as important to overall device efficiency as principal light absorption. Fullerenes are a class of molecules composed entirely of an interconnected network of pentagonal and hexagonal all-carbon rings, making them one of several pure allotropes of carbon. The simplest fullerene, sometimes referred to as buckminsterfullerene or bucky-ball due to its resemblance to a soccer ball, takes the form of a hollow sphere with the formula C_{60}. Like P3HT, The cage structure of C_{60} is conjugated with alternating single and double bonds.

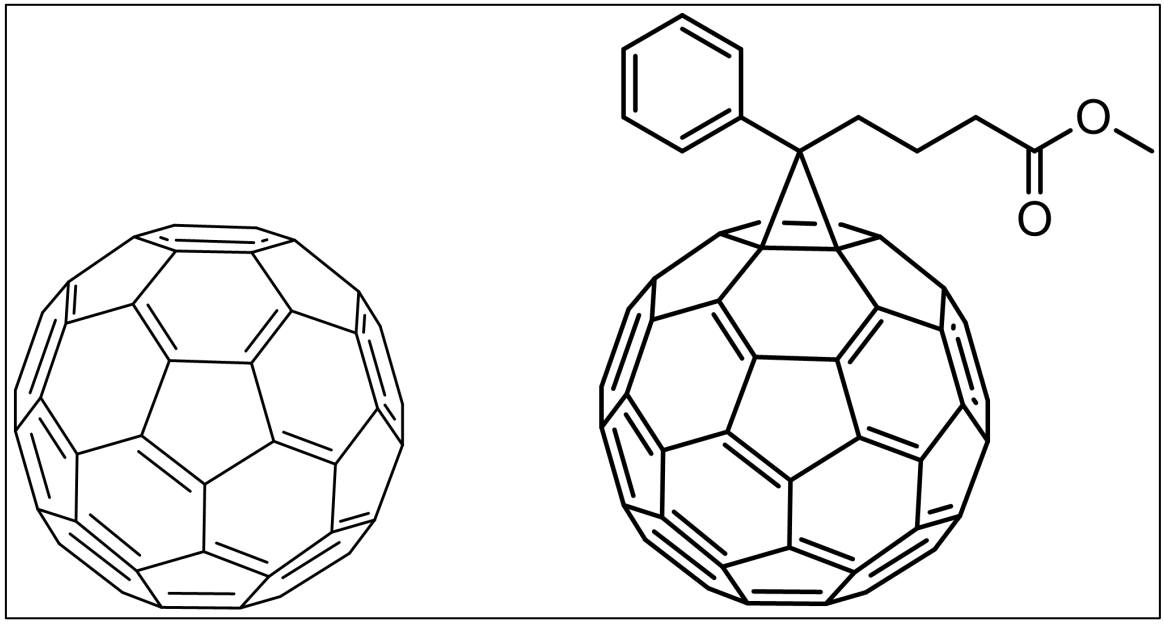

Figure 7: Structures of C_{60} (left) and PCBM (right).

[6,6]-phenyl C_{61}-butyric acid methyl ester (PCBM) is perhaps the most studied fullerene in the field of plastic solar cell and like most fullerene derivatives, is a great electron acceptor owing to its low reorganization energy.[21] While early OPVs adopted a bilayer

arrangement with an evaporated layer of C_{60} on top, PCBM's increased solubility in organic solvents provides a solution processable alternative route to device fabrication.[22]

P3HT and PCBM are both molecular semiconductors. Delocalized π states arising from these conjugated systems make up their frontier electronic bands and determine corresponding band gap. Here, the band gap describes the difference in energies between the highest occupied molecular orbital (HOMO) and lowest unoccupied molecular orbital (LUMO) on the molecule. This is analogous to the energetic difference between the valence and conduction band in a semiconductor like silicon. The energy levels and optical band gaps of P3HT and PCBM are precisely tuned so that the two materials function as an electron donor and acceptor in the active layer of an organic photovoltaic (or photoelectrode). A schematic diagram of their band energies is shown in Figure 8.

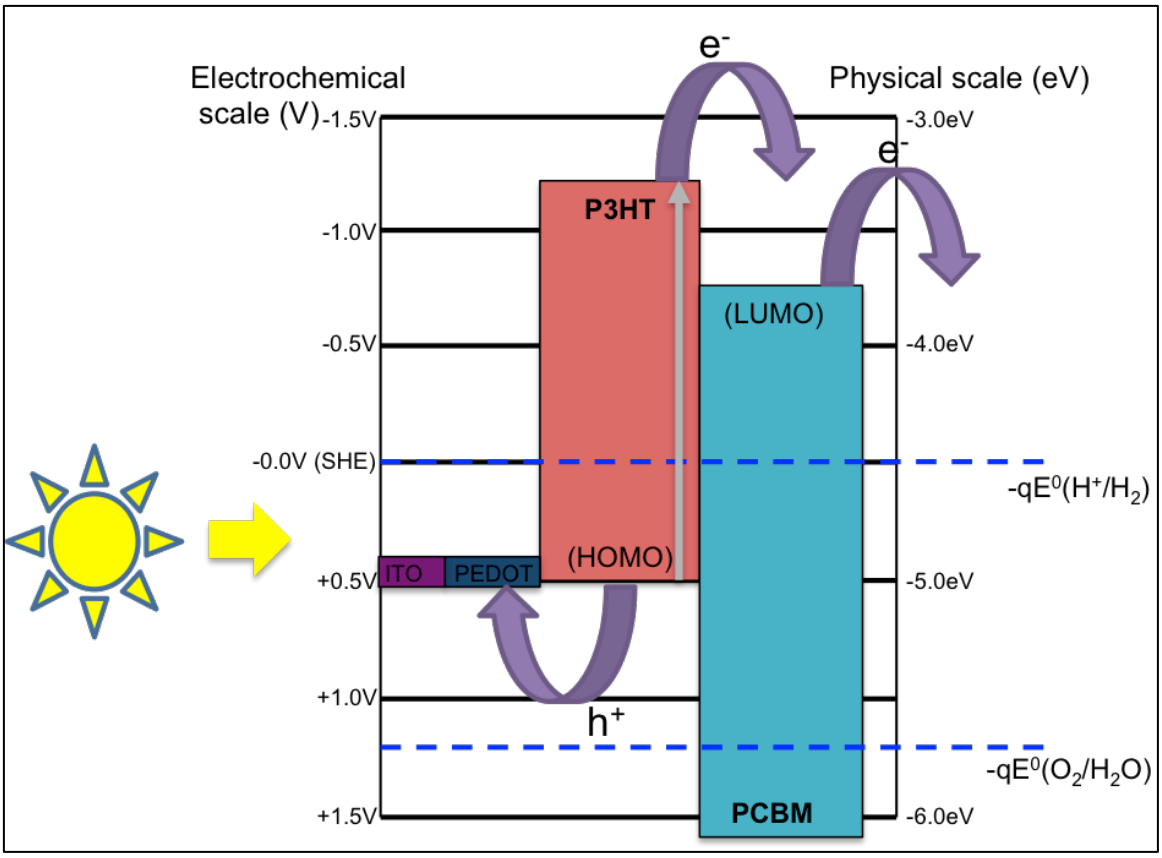

Figure 8: Band energy diagram showing photoexcited electron transfer from P3HT to PCBM with energy levels for relevant water splitting half reactions indicated by dotted blue lines. ITO and PEDOT are included as examples of an anode contact and hole transport layer, respectively. HOMO/LUMO levels reported from Sigma Aldrich.

The p-type donor (P3HT) is the principal light absorber. Upon irradiation with energy equal to or greater than the band gap, photoexcitation of an electron (e^{-1}) into the LUMO (conduction band) will occur, leaving behind an empty valance in the HOMO, designated as an electron hole (h^{+}). The photogenerated electron-hole pair is bound by coulombic forces and forms a pseudoparticle referred to as an exciton. The n-type acceptor (PCBM) has an energetically lower-lying LUMO level, making it favorable to accept the excited electron from the donor. Holes will then move through the p-type material towards the anode (ITO with PEDOT as a hole transport layer) while electrons

migrate to the cathode (H^+/H_2 acts as electrical contact here) through the n-type semiconductor. The difference in work functions between the anode and cathode create an intrinsic electric field that helps extract the free charge carriers. The open circuit voltage (V_{oc}) is determined by the difference in these work functions, or when matched appropriately, by the donor:acceptor junction in the bulk blend. That is to say, the energy difference between the HOMO level of the p-type donor and the LUMO level of the n-type acceptor dictates the maximum attainable V_{oc}. For most polymer solar cells, the produced open circuit potentials are in the range of 0.5-1.0 V.[23,24]

Because generated excitons must diffuse to a donor:acceptor interface before charge separation can occur, the active layer design places a limit on the efficiency of the cell. Excitons in polymer:fullerene systems typically have diffusion lengths on the order of 5-10 nm.[25] The diffusion length is the average distance excitons move between generation and recombination. This means excitons generated more than 10 nm on average from a P3HT:PCBM junction are less likely to separate into an electron and hole, ultimately limiting the observed photocurrent. For this reason, the best active layer structure is not a bilayer because the majority of the light-harvesting material will not be sufficiently close to a donor:acceptor interface for charge extraction to occur. Instead, one of the simplest and most effective approaches happens to involve the blending of the donor and acceptor together in solution. The active layer can then be cast from this mixture of both species. As the film dries, the two materials will separate into distinct phases that are evenly distributed (ideally) throughout the three-dimensional bulk of the active layer. Such device architecture is referred to as a bulk heterojunction (BHJ). The morphology of bulk heterojunctions can be probed using a variety of noninvasive optical

techniques such as ellipsometry.[26] Ellipsometry is a sensitive method used to study polarization changes in light reflected from a surface. Observed changes in polarization are evidence of direct properties of the bulk sample such as thickness and refractive index. A schematic of a complete layer stack for a bulk heterojunction solar cell is shown in Figure 9.

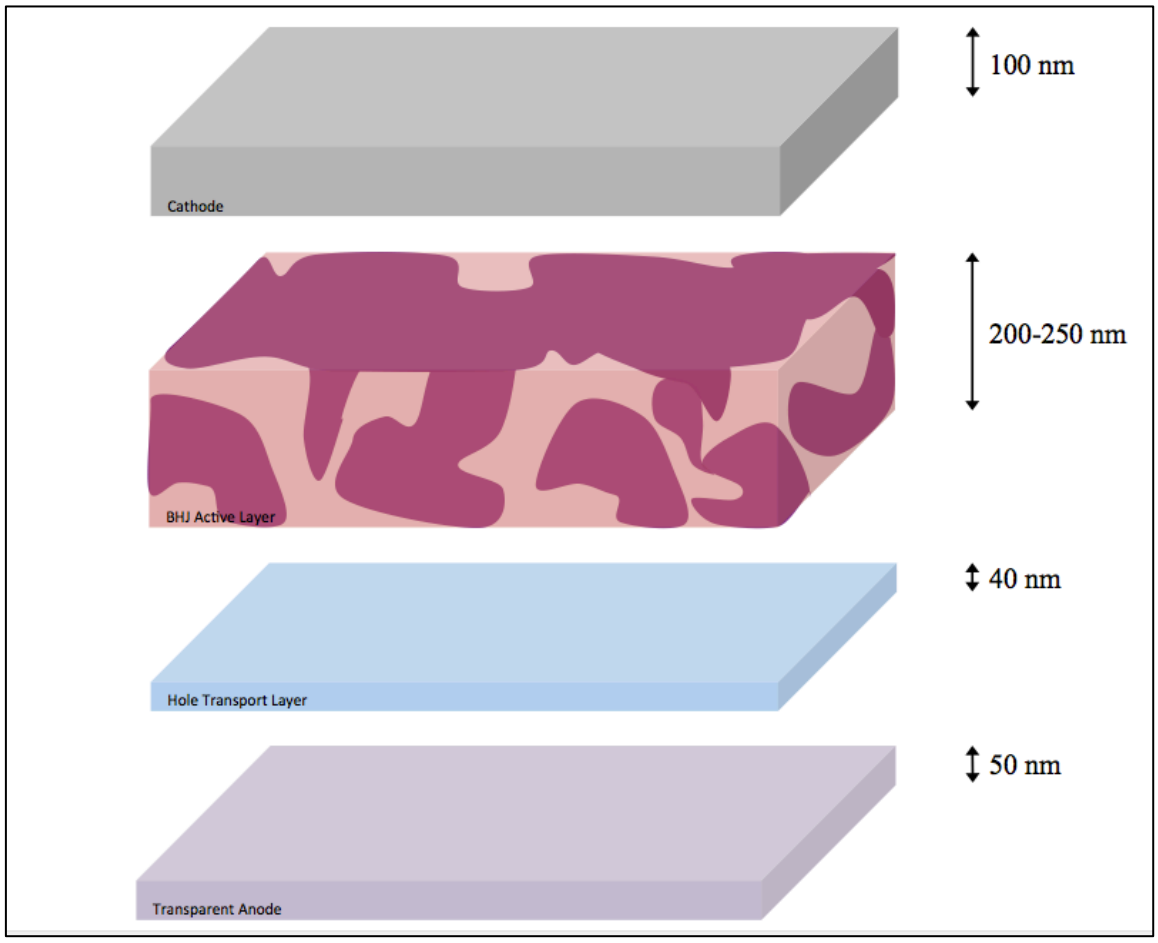

Figure 9: Stacked arrangement of a BHJ architecture including representative layer thicknesses as reported in the literature.[27]

The photoactive portion of the device is illuminated through the transparent anode, which is usually a thin layer of a conductive oxide such as ITO (indium oxide

with high amounts of tin dopant). A hole transport interlayer like poly(3,4-ethylenedioxythiophene) poly(styrenesulfonate) (PEDOT:PSS) may be added to help facilitate hole injection at the anode and improve electrical contact to the active layer. The BHJ is responsible for exciton generation and charge separation. In a solar cell, holes will collect at the anode while electrons move through the n-type semiconductor towards the cathode and an external circuit. However, to create a bulk heterojunction PEC, the (H^+/H_2) redox couple acts as the top electrical contact and electrons will flow into solution and drive the reduction of protons to molecular hydrogen.

The interactions and efficient charge transfer between the p-type donor P3HT and n-type acceptor PCBM are well characterized in bulk heterojunction organic photovoltaics.[20] Constructed BHJ solar cells also consistently outperform similar bilayer arrangements.[28] P3HT:PCBM blends also demonstrate considerable heat resistance as blends are typically annealed at temperatures up to 180^{o}C.[29]

Despite widespread use in OPVs, the BHJ architecture is noticeably underrepresented in the area of photocatalysis. At the time of this study, there are few accounts of organic semiconductor systems in contact with aqueous media for catalytic hydrogen production. [30,31,32] While these reports achieve open circuit voltages comparable to the same materials in OPVs, the corresponding photocurrents are often quite low (aprox. 0.03 mA cm^{-2} at -0.8 V vs. reference) and ultimately limit cell efficiency.[32] To enhance the photocurrent (and subsequently, solar-to-hydrogen efficiency) a catalytic layer of platinum has been added to the surface of the photoelectrode.[30,32]

1.5 Catalysis of the Hydrogen Evolution Reaction

An ideal HER catalyst must not only promote H_2 production, but also do so at modest overpotentials. Platinum is an extremely valuable noble metal with a variety of uses derived from its resistance to corrosion. The low reactivity of this metal is directly related to its applications in catalysis and the hydrogen evolution reaction specifically. The Sabatier principle adequately explains this relationship; the ideal interaction between a catalyst and its substrate should be "just right".[33] A perfect HER catalyst is therefore one that can adsorb (and desorb) H_2 easily. If the interaction is too weak, the substrate (H^+, in this case) will not be able to bind effectively. Likewise, if the interaction is too strong, the HER catalyst will be blocked by a product that is unable to dissociate. This relationship can be represented graphically using what is known as a volcano plot, where the peak of the plot represents the target "Goldilocks zone" of catalyst activity. A volcano relation evaluating transition metals for possible HER activity is shown below.

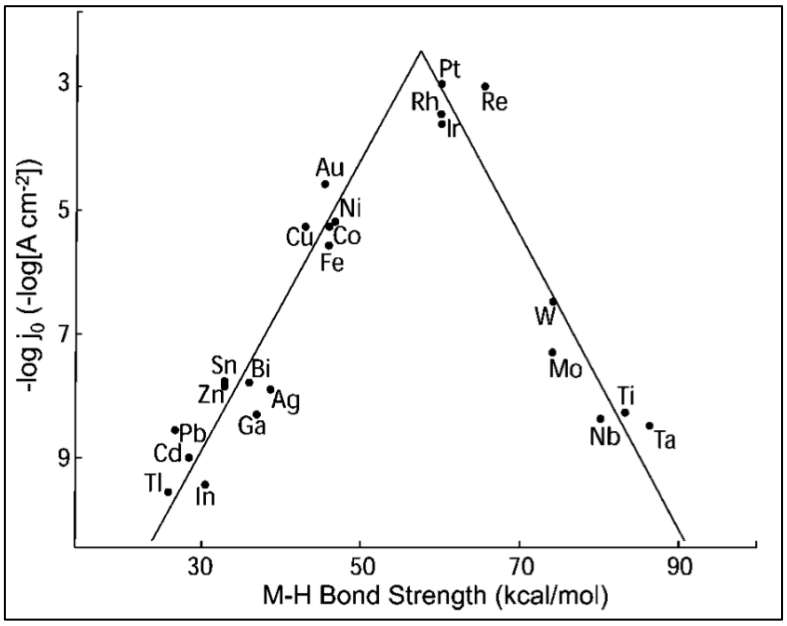

Figure 10: Volcano plot for pure metals in acidic solution[34]

Figure 10 shows the produced current density as a function of the metal-hydrogen bond strength for a series of transition metals.[34] Clearly, noble metals (Pt, Rh, Ir, Au, etc.) exhibit the highest activity. In fact, platinum wire constitutes the basis of a standard hydrogen electrode (SHE) as a result of its ability to drive the HER at the lowest applied overpotentials. Metals like nickel, cobalt and molybdenum appear to be the most active non-precious metals. While many new materials (such as NiMo[35], CoP[36] and MoS_2[37]) have been engineered as more earth-abundant alternatives, platinum is still widely regarded as the most active HER catalyst due to its high work function and near-negligible hydrogen adsorption free energy. [34,38]

Electrochemical measurements (JV data) can give valuable insight into the characteristics of a catalyst and the mechanisms that take place on its surface. Tafel plots are constructed to describe catalytic performance. The Tafel relationship (equation 5, below) relates the overpotential as a function of the log of the current density.[13]

$$\eta = b \log (J/J_0) \tag{5}$$

Here, η is the overpotential (V), J is the produced current density (A cm^{-2}), and J_0 is the exchange current density (A cm^{-2}). The term b represents the so-called Tafel slope and dictates the increase in voltage required to increase the observed current by one order of magnitude (reported in mV $decade^{-1}$). Extrapolation of the linear portion of the curve to the x-axis allows us to calculate the exchange current density (equilibrium current at $\eta = 0$). J_0 can be thought of as the current where the forward (cathodic) and reverse

(anodic) reactions are balanced on the surface of the electrode and no net current change is observed. Calculation of J_0 gives insight into catalyst performance; it has been shown that the maximum exchange current density arises when the hydrogen adsorption free energy is close to zero.[39] The volcano plot in Figure 10 relates the exchange current density (-log [A cm^2]) as a function of metal-hydrogen bond strength (kcal mol^{-1}). Changes in the Tafel slope are indicative of changes in catalyst activity and account for mechanistic variations at different overpotentials. Under acidic conditions, the mechanism of hydrogen evolution on a catalyst surface can be broken down into three elementary steps.[39]

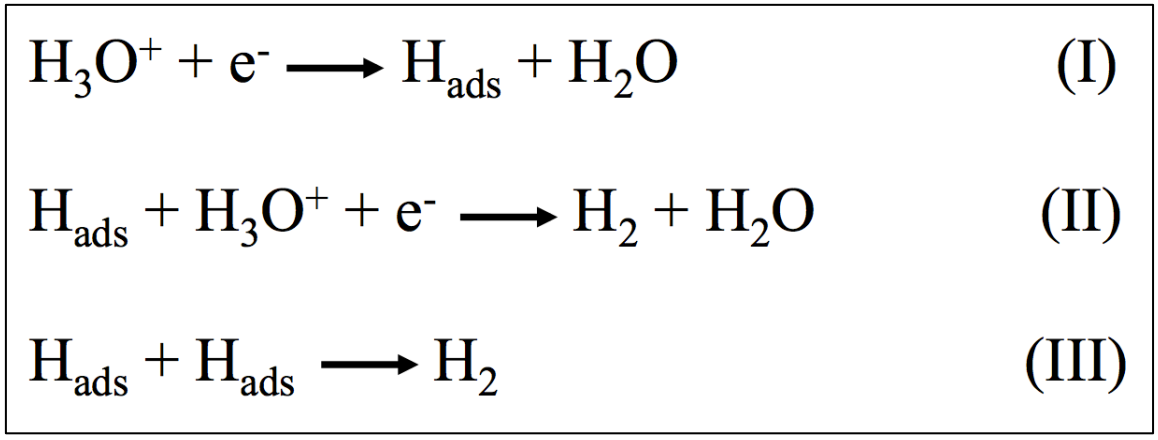

Figure 11: Processes involving the role of chemisorbed hydrogen that determine HER reaction kinetics as reported by Conway et al.[39]

In the initial discharge step (Volmer reaction, I), the H_3O^+ ion is the proton source and deposits a H atom on the metal surface (H_{ads}). This is followed by either an electrochemical desorption (Heyrovsky reaction, II) or a H_{ads}-H_{ads} combination step (Tafel, III). It has been reported in the literature that the Tafel slope should fall around 120, 40, or 30 mV dec^{-1} when the rate-limiting step is I, II, or III, respectively.[39–42]

For these reasons, researchers often employ both J_0 and b to interpret whether changes in electrode performance are due to electronic, structural, or combined effects of the catalyst.

1.6 A Catalyst-coated BHJ Photocathode

A bulk heterojunction based on the well-studied P3HT:PCBM blend is sufficiently energetic to produce the photovoltage needed to drive molecular hydrogen evolution in acidic media. Furthermore, this polymer-fullerene arrangement represents a cheap, visible-light driven system with the potential for industrial scalability (screen printing and roll-to-roll processing) on flexible substrates. However, due to slow reaction kinetics at the semiconductor/water interface, the addition of a heterogeneous HER catalyst like platinum is necessary to more effectively shuttle electrons to the (H^+/H_2) couple and boost the observed photocurrent. We choose to synthesize 3-5 nm platinum nanoparticles (PtNPs) for use as the embedded electrocatalyst for four reasons. First, a nanoscale catalyst possesses a much higher effective surface area than the bulk metal. Because catalytic efficiency is directly related to exposed surface sites, this is extremely advantageous. Second, this route substantially reduces the quantity of the precious metal used. Third, a porous catalyst layer allows the electrolyte solution to diffuse around the nanoparticles and touch the organic phase. This should allow the redox potential of the solution to act like a metal contact at the semiconductor/aqueous interface and help drive charge extraction. Finally, solvent-dispersible PtNPs permit solution deposition of the catalyst layer, thereby creating a totally solution-processable photoelectrode. Figure 12 shows the final catalyst-coated device architecture.

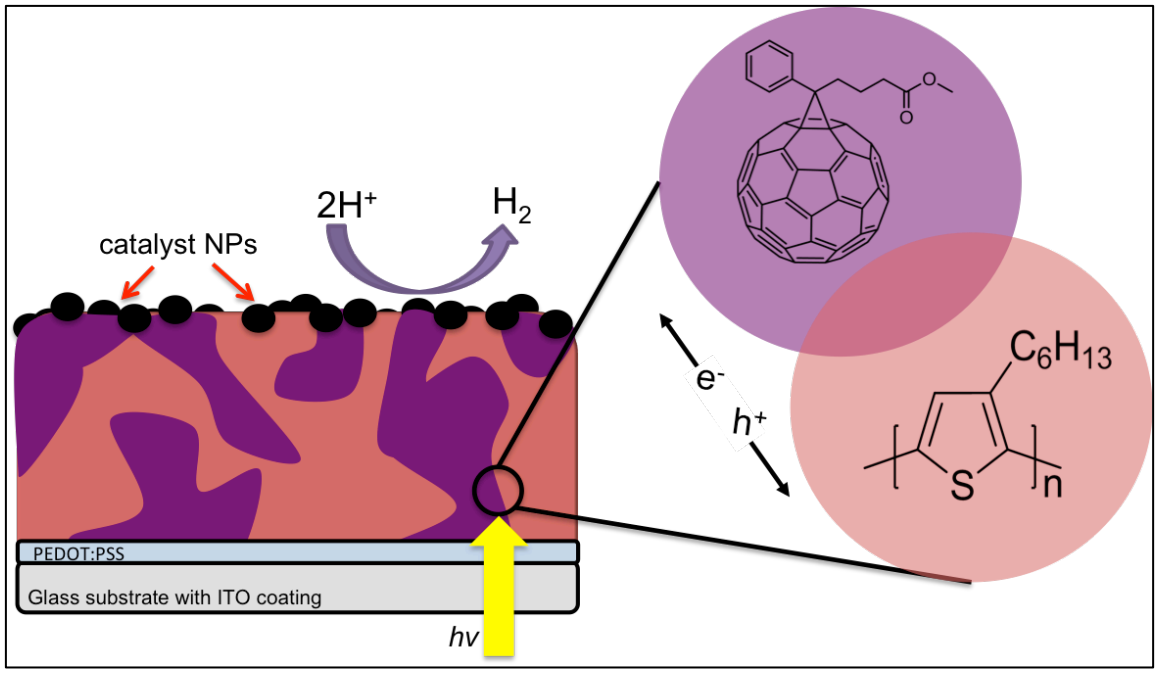

Figure 12: Schematic representation of the final bulk heterojunction photocathode with catalytic islands of nanoparticles.

Once again, the appeal of this design lies in the ability to readily cast each phase layer-by-layer. Because the nanoparticle layer coats the BHJ surface, light must enter through the transparent glass substrate. A thin film of ITO constitutes the anodic contact and poly(3,4-ethylenedioxythiophene) poly(styrenesulfonate) (PEDOT:PSS) forms the hole transporting layer. These two materials are largely transparent to visible light. Once illuminated in the active phase, electrons will transfer from the P3HT donor to PCBM and move through this acceptor material towards the aqueous interface where they are trapped on surface of the Pt catalyst particles. Consequently, PtNPs on the surface of exposed P3HT should not contribute to H_2 generation. Partial diffusion of PtNPs into the bulk should not pose issue as this has actually been shown to facilitate charge transfer and improve power conversion efficiencies in OPVs.[43,44]

In order for a system with so many components to perform optimally, electrical contact between the photoactive portion, metal catalyst and electrolyte solution must be maintained and understood. Interactions at the semiconductor, catalyst, and aqueous interfaces will ultimately determine and limit device efficiency and longevity.

1.7 Calculations and Measurements of Solar Conversion Efficiencies

In the 1995 issue of *Accounts of Chemical Research*, several "Holy Grails in Chemistry" were proposed, including Allen Bard's definition of the water splitting holy grail[45]:

> *"We want an efficient and long-lived system for splitting water to H_2 and O_2 with light in the terrestrial (AM1.5) solar spectrum at an intensity of one sun. For a practical system, an energy efficiency of at least 10% appears to be necessary. This means that the H_2 and O_2 produced in the system have a fuel value of at least 10% of the solar energy incident on the system."*

At present, state-of-the-art PECs are able to achieve only a fraction of the 10% goal proposed by Bard but development is progressing.[46,47] The main barriers limiting efficiency are primarily material related (rapid recombination of free-charge carriers, poor visible light sensitivity and improperly aligned band edges).[47]

The overall efficiency (η) for a water splitting photoelectrode assuming no device corrosion and operating at a faradaic efficiency of unity can be readily calculated from its current-voltage data as follows using equation 6.

$$\eta = \frac{J_{mp}(1.23V - V_{app})}{P_{in}} \quad (6)$$

Here, V_{app} is the applied voltage between the photoanode (water oxidation) and photocathode (hydrogen reduction), J_{mp} is the measured photocurrent density and P_{in} is the illuminated power intensity (typically taken to be 100 mW cm^{-2} at 1 sun).[13] To separately evaluate the conversion efficiency of an individual half-cell (photoanode or photocathode), a similar set of equations may be used. This allows for the calculation of a true solar-to-hydrogen (STH) efficiency from the JV characteristics of a single hydrogen evolving photocathode. Such an arrangement is beneficial to the optimization of the half-cell as it prevents interference from the reverse reaction (i.e. H_2 oxidation). When characterizing only a single cell, the open circuit voltage (V_{oc}) and short circuit current density (J_{sc}) must be referenced to the thermodynamic potential of either water splitting half-reaction (H^+/H_2 or O_2/H_2O) at a specific pH.[13] The half-cell efficiencies (η) are calculated similarly using equations 7 and 8.

$$\eta = \frac{J_{mp}V_{mp}}{P_{in}} \tag{7}$$

$$ff = \frac{J_{mp}\,V_{mp}}{J_{sc}\,V_{oc}} \tag{8}$$

J_{mp} and V_{mp} are the current density and voltage at the maximum power point and P_{in} is the power intensity of the incident light. The fill factor (*ff*) represents the maximum power output divided by the product of the open circuit voltage and short circuit current.

To obtain these key parameters, a three-electrode setup (with voltage measured vs. a standard reference) submerged in an electrolyte solution of known pH with

hydrogen bubbled and under an illumination of 1 sun is desired. Saturation of gaseous hydrogen is extremely important for reliable measurements. It is important to have both oxidized and reduced species present in solution at constant concentrations to ensure a stable Nernstian potential for accurate V_{oc} measurements of a H_2 evolving photocathode. Additionally, bubbling hydrogen improves the experimental analogue, as any working device continuously generating hydrogen will saturate with the gas. Under these conditions, measurement of cathodic current (electrons flow to the H^+/H_2 redox couple contact) can be directly correlated to molecular hydrogen production.

CHAPTER 2: EXPERIMENTAL

2.1 Materials, Methods and Instrumentation

2.1.1 Purchased Reagents and Chemicals

Poly(3-hexylthiophene) (P3HT) and [6,6]-phenyl C_{61}-butyric acid methyl ester (PCBM) were obtained from Sigma Aldrich and used as received. Poly(3,4-ethylenedioxythiophene) poly(styrenesulfonate) (PEDOT:PSS; Clevios AI4083) was purchased from Ossila and filtered using a cellulose acetate syringe (0.45 μm pore diameter) filter prior to use. Non-patterned tin-doped indium oxide (ITO) were acquired from Ossila (sheet resistance = 18-20 Ω sq^{-1}).

Platinum (II) acetylacetonate, 1,2-hexadecanediol, oleic acid (technical grade, 90%), oleylamine (approximate C18 content 80-90%), dioctyl ether (99%), ethyl alcohol (190 proof, ACS grade), and glacial acetic acid were purchased from Sigma Aldrich and used without further purification.

2.1.2 Instrumentation and Techniques

Electrochemical measurements were performed using a Gamry Reference 600 potentiostat. Typical photoelectrode setup consisted of our fabricated working electrode (either PtNPs on ITO or BHJ photoelectrode), a Ag/AgCl reference and a platinum foil counter electrode submerged in 0.5 M H_2SO_4 (semiconductor grade, purchased from Sigma Aldrich) with constant stirring. H_2 was bubbled into solution continuously to maintain saturation and a well-defined H^+/H_2 redox potential. Devices were illuminated

through the transparent ITO side using a Xe-arc lamp with a calibrated power intensity of 100 mA cm^{-2}. Linear sweep voltammetry (LSV) and cyclic voltammetry (CV) were carried out at room temperature with a scan rate of 50 mV s^{-1}, unless otherwise noted. Electrode areas were calculated using the pixel-counting software ImageJ64. UV-Visible absorbance profiles were acquired on a Cary 300 Bio UV-Visible spectrophotometer. Thermogravimetric analysis was performed with a Mettler Toledo TGA SDTA851e. A Perkin Elmer Spectrum 100 FT-IR was used for infrared (IR) spectroscopy analysis. Morphology of the nanoparticle catalysts was studied on a LaB_6 JEOL 2100 Transmission Electron Microscope (TEM) with an Oxford INCA EDX system. Thicknesses of photoactive layers were measured from film cross-sections using a Raith 150 Scanning Electron Microscope (SEM).

2.2 Synthesis of Pure Platinum Nanoparticles

3-5 nm platinum nanoparticles (PtNPs) were synthesized following an modified procedure originally reported by Sun et al.[48] as follows. In a standard synthesis, $Pt(acac)_2$ (200 mg, 0.5 mmol) and 1,2-hexadecanediol (390 mg, 1.5 mmol) were combined in dioctyl ether (30 mL) and stirred while heating to approximately 180 ^oC to dissolve components. The surfactants oleic acid (0.16 mL, 0.5 mmol) and oleylamine (0.17 mL, 0.5 mmol) were then injected and the reaction was heated to reflux (approx. 286 ^oC for dioctyl ether) and maintained at this temperature for 30-40 min. The solution turned from pale yellow to brown/black at this point. The heat was then removed and the solution allowed to cool to room temperature over the course of several hours.

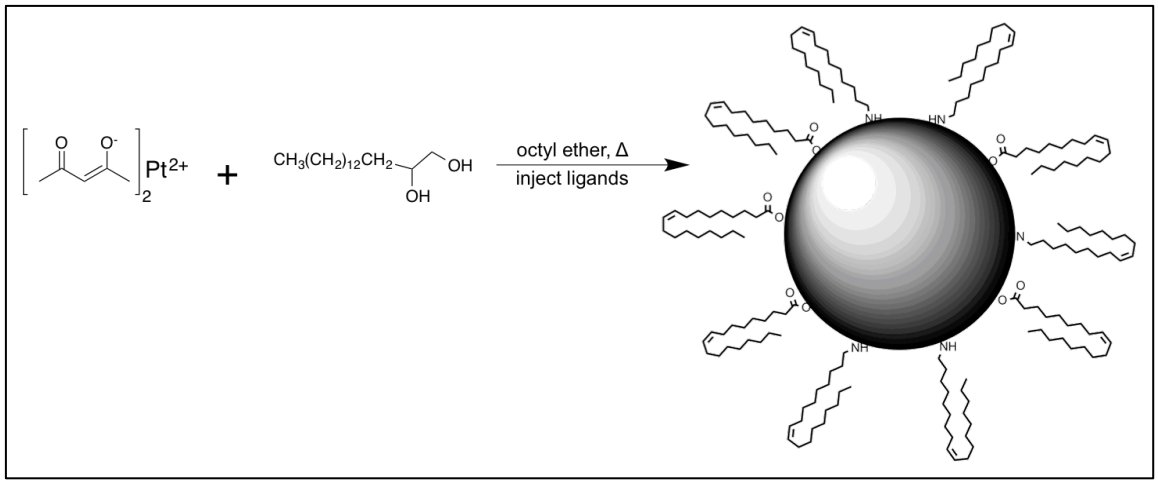

Figure 13: Synthesis of PtNPs involves the reduction of a platinum salt by 1,2 hexadecanediol in a high boiling point organic solvent. Oleic acid and oleylamine are injected as capping agents.

PtNPs were extracted from the reaction mixture by centrifugation. This was typically accomplished by combining small fractions of the reaction mixture with three times the volume of ethanol and centrifuging at 2000 rpm for two hours. A small amount of a co-solvent such as hexanes (1-2 mL) was also added as necessary to maintain phase miscibility. The pale yellow supernatant could then be discarded. After one wash, approximately 125 mg (on average) of the pure Pt nanocrystals could be isolated as a black solid. This crude product was re-dispersed in a small volume of hexanes and designated "untreated PtNPs" for subsequent tests.

2.3 Surfactant Removal Methods for PtNPs

2.3.1 Heat Treatment

Thermal treatment to liberate weakly bound surfactants from metal nanoparticles has been previously reported.[49] After drying under vacuum, samples of untreated PtNPs (250 μg) on ITO were heated in a furnace for 30 min at 150, 200 and 280 ^{o}C. Thermal removal of bound ligands was carried out in air.

2.3.2 Ethanol Wash and Centrifugation

To carry out the ethanol (EtOH) wash step, approximately 50 mg of untreated PtNPs was dried in a vacuum oven, split into three centrifuge tubes and filled with 15 mL of EtOH. Each tube was sonicated for several minutes to disperse the PtNPs prior to immediate centrifugation for 2 h at 4000 rpm. After discarding the supernatant, each tube was refilled with 15 mL of fresh EtOH and sonicated to re-disperse the NPs before returning to the centrifuge. It is important to note that the pale yellow color of the supernatant disappeared after 3-4 washes and sonication as a dispersal technique became increasingly difficult after 5 washes. Aliquots containing approximately 10 mg of material were collected after 5 and 10 subsequent washes, dried under vacuum and dispersed in hexanes as 10 mg mL^{-1} suspensions.

2.3.3 Stir in Acetic Acid

50 mg of dry, untreated PtNPs were placed in a clean 50 mL round bottom flask with 15 mL of glacial acetic acid. The solution was gently heated (60 ^{o}C) and vigorously stirred (1000 rpm) for several hours. 5 mL portions were collected after 2, 5 and 24 hours. To remove the acetic acid, EtOH was added and the product collected after one centrifugation cycle. After drying under vacuum, each fraction was dispersed in hexanes at a concentration of 10 mg mL^{-1}.

2.4 Organic Film Preparation

Indium tin oxide (ITO) coated glass slides (18-20 Ω sq^{-1}) were cleaned by successive sonication in alconox, acetone, isopropanol and DI water, followed by UV O_3 (BioForce UV/Ozone procleaner) treatment for 30 min. Typical film preparation then proceeded accordingly: A thin layer of PEDOT:PSS (45 μL, filtered prior to use) was

spin-cast onto a clean ITO substrate at 2000 rpm and thermally annealed (150 ^{o}C , 20 min), leaving a partially transparent thin film. A pre-mixed (1:1 by weight, 20 mg mL^{-1}) solution of P3HT:PCBM in 1,2-dichlorobenzene was similarly deposited atop the PEDOT:PSS layer by spin coating at 2500 rpm for 45 s followed by 3000 rpm for 60 s. Films were then annealed at 180 ^{o}C for 25 min. Both film deposition and thermal annealing was carried out under a N_2 atmosphere. Thickness of the P3HT:PCBM active layer was confirmed to be 250-300 nm by cross-sectional SEM.

2.5 Electrode Assembly and Encapsulation

Catalyst-only devices were prepared by drop-casting PtNP suspensions from a dispersion in hexanes onto clean ITO on a flat surface (Figure 14.a). Depositing 25 μL of 10 mg mL^{-1} PtNP suspension in hexanes gave a catalyst mass loading of 250 μg per area. Electrode surface area was also controlled between device series. To coat the catalyst onto the P3HT:PCBM film (Figure 14.b), PtNPs were identically deposited via drop-casting in air, giving a final device architecture of ITO/PEDOT:PSS/P3HT:PCBM/PtNPs (Figure 14.c).

To provide anodic contact to the underlying ITO, a portion of the top layer was wiped away with an appropriate solvent and a thin silver wire was connected to the exposed oxide surface using conductive silver paint (Figure 14.d). Electrodes were encapsulated with *LOCTITE*© marine epoxy (Figure 14.e) to protect the sensitive conductive oxide and hygroscopic PEDOT:PSS layers from contact with the acidic solution once submerged. The completed photoelectrodes were placed in a desiccator blanketed with argon while the protective coating was allowed to dry and harden overnight.

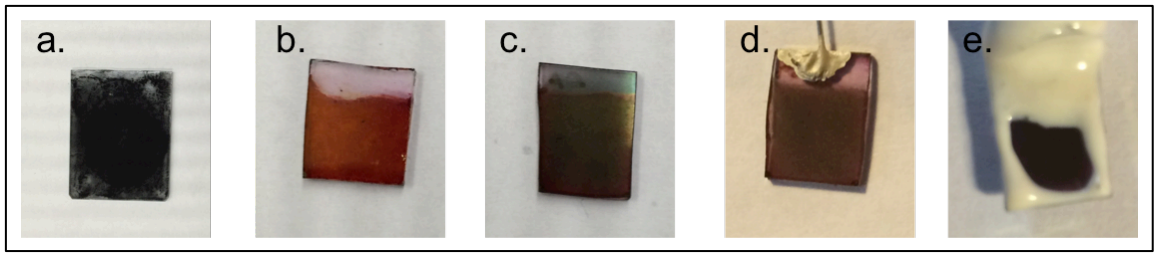

Figure 14: Images of ITO/PtNPs (a), ITO/PEDOT:PSS/P3HT:PCBM (b), ITO/PEDOT:PSS/P3HT:PCBM/PtNPs (c), wire contact to ITO (d), and the final encapsulated photoelectrode (e).

CHAPTER 3: RESULTS AND DISCUSSION

3.1 Final Device Architecture and Characterization

3.1.1 Cross-Sectional SEM of Bulk Heterojunction

A sample film of 1:1 P3HT:PCBM was deposited on ITO by spin coating 35 μL of a 20 mg mL^{-1} solution at 2500 rpm for 45 s followed by 3000 rpm for 60 s and thermal annealing step at 180 ^{o}C for 30 min. The substrate was then broken through the ITO side and mounted vertically in a scanning electron microscope in order to obtain the film cross section (Figure 15). Using the pixel counting program ImageJ64, layer thickness was measured to be approximately 260 nm.

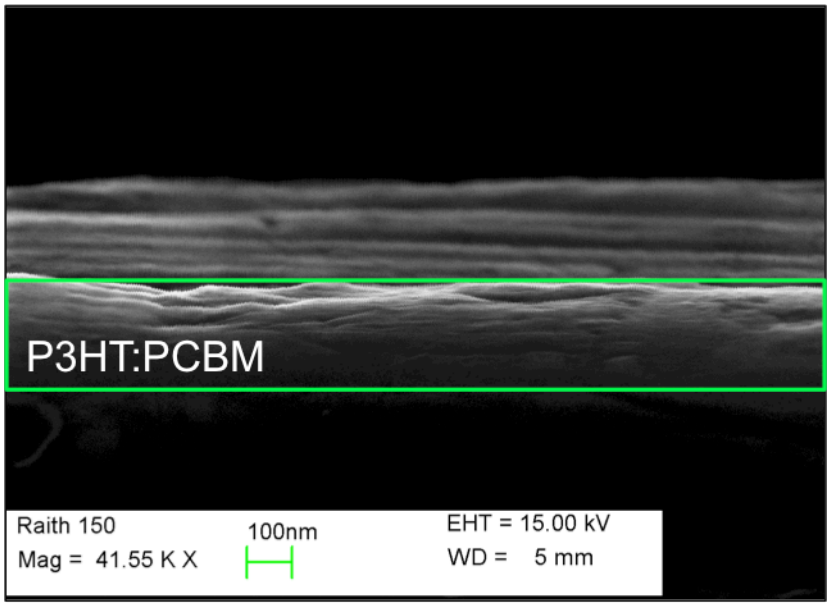

Figure 15: SEM cross-section of a 1:1 P3HT:P3BM on ITO. The green box highlights the film in the foreground.

3.1.2 Transmission Electron Microscopy of PtNPs

Platinum nanocrystals are well-characterized structurally and have been prepared in a variety of solvents with a diverse range of shapes and sizes.[50–54] For our purposes, colloidal platinum nanoparticles were synthesized by modifying a procedure reported by Sun et al.[48], therefore making structural corroboration necessary. Transmission electron microscopy (TEM) confirms our PtNPs to be monodisperse with and average particle diameter of 3-5 nm (Figure 16 a and b).

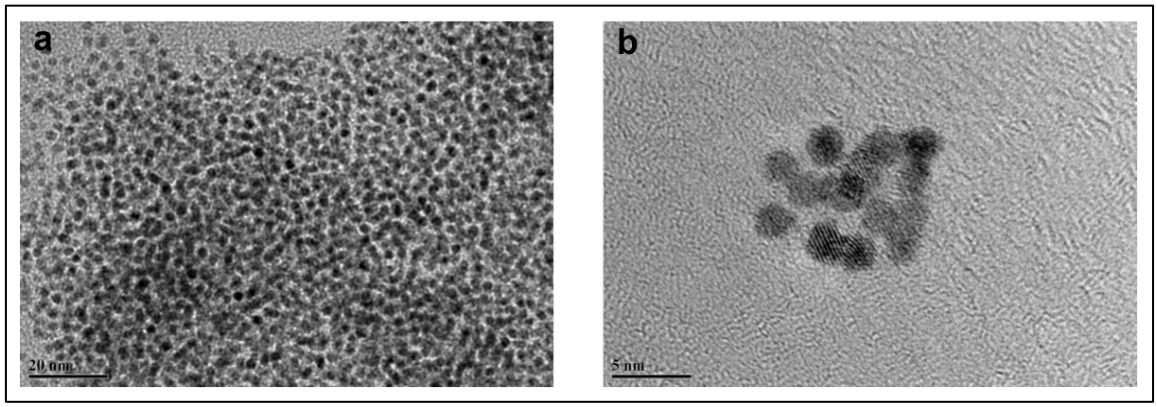

Figure 16: TEM images of as-sensitized Pt NPs showing size, shape and distribution from a scale of 20 nm (a) and 5 nm (b).

Additionally, Energy-dispersive X-ray (EDX) spectroscopy was employed to confirm the elemental composition of the nanoparticles. Because each element has a unique electronic structure, the X-ray emission profile is a vital tool in elemental analysis. Figure 17 shows the EDX spectra of our as-synthesized PtNPs.

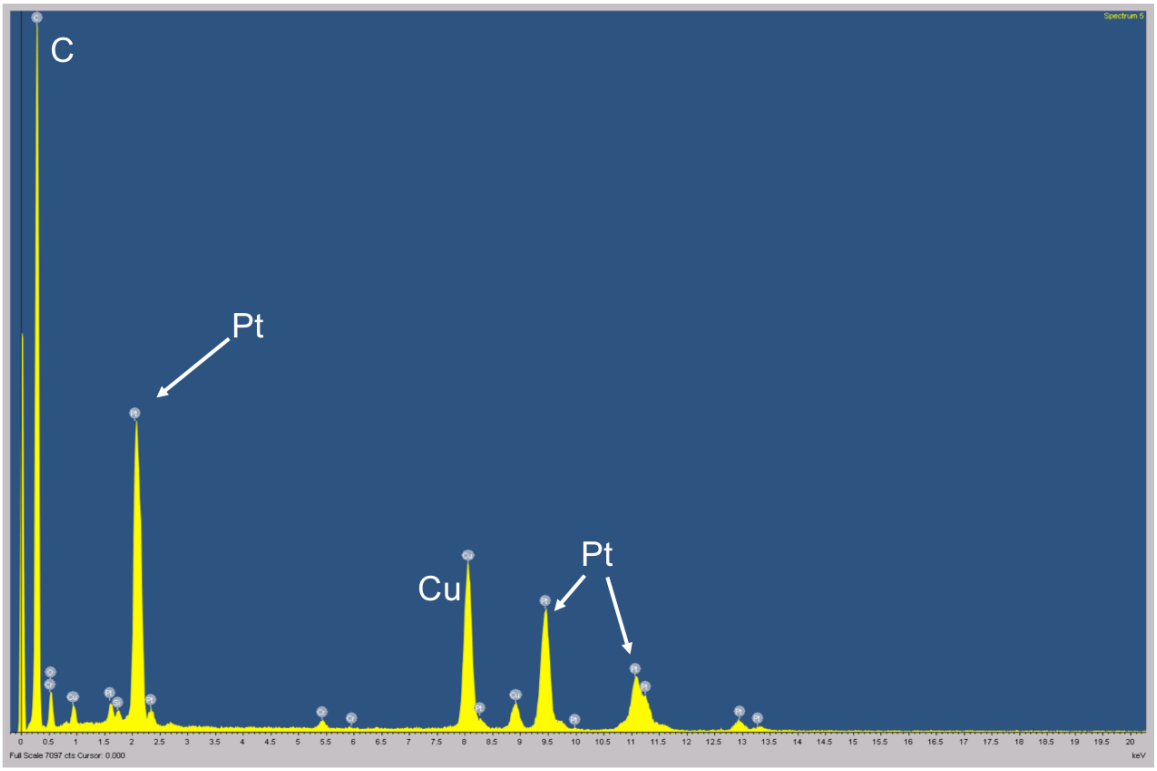

Figure 17. EDX Spectra with peak size showing relative abundance of select elements. Y-axis measured in keV.

The first major peak is primarily due to the carbon mesh support for the sample while the peak for copper arises from the copper TEM grid. Platinum is clearly present. Some of the carbon abundance may come from the presence of bound organic ligands on the surface of the platinum particles. Other trace elements can be attributed to small impurities on the detector.

3.2 JV Characteristics of Untreated PtNPs

The current-voltage (JV) characteristics of our platinum nanoparticle catalyst were first evaluated against two standard benchmarks- a Pt button electrode and bare ITO. The bare ITO electrode represents the catalytic capacity of our conductive substrate by itself. A polished platinum button is included in order to reference the catalytic capacity of our nanoparticles to the bulk metal.

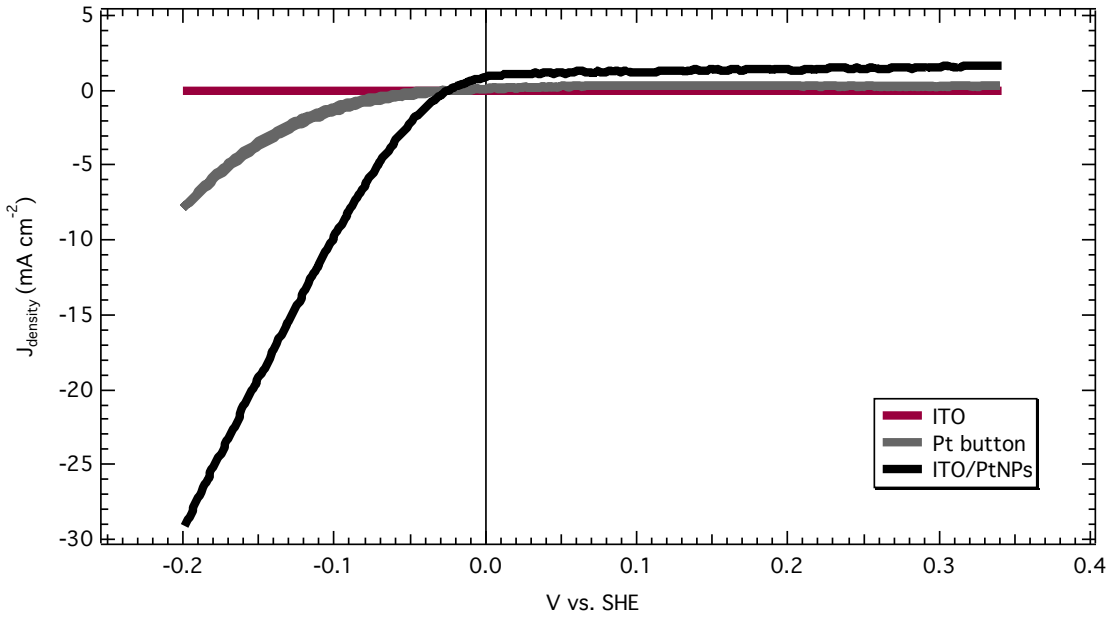

Figure 18. Linear sweep voltammogram of a thin layer of PtNPs on ITO compared to plain ITO and a Pt button electrode. Recorded with a scan rate of 20 mV s^{-1} in 0.5 M H_2SO_4 with constant stirring and H_2 saturation.

From the figure above, it is clear that the thin layer of the Pt nanoparticles produces a higher current density (approx. 28 mA cm^{-2} at -200 mV vs. SHE) at the same applied overpotential when compared to the bulk metal (roughly 8 mA cm^{-2} at -200 mV vs. SHE), which is known to be an extremely active HER catalyst. On the other hand, the solitary ITO electrode (representative of a non-catalytic conductive substrate) produces almost no measurable change in current when a bias of -200 mV is applied. Using a nanoparticle catalyst helps maintain porosity and allows electrolyte to diffuse around the catalyst and contact all of the exposed surface area. This results in much higher current densities for our PtNPs compared to bulk platinum. It is noteworthy that some oxidative (positive) current is observed on the PtNP test, possibly due to electrochemical equilibration on the surface of the surfactant-covered nanoparticles.

Stability is a critical parameter when evaluating practical electrode performance and therefore warrants investigation. Two important techniques to assess an electrode's catalytic tolerance over time are cyclic voltammetry and chronoamperometry. Cyclic voltammetry (CV) involves sweeping across a potential range for multiple cycles. Figure 19 shows a cyclic voltammogram for a near identical ITO/PtNP electrode evaluated after many scans.

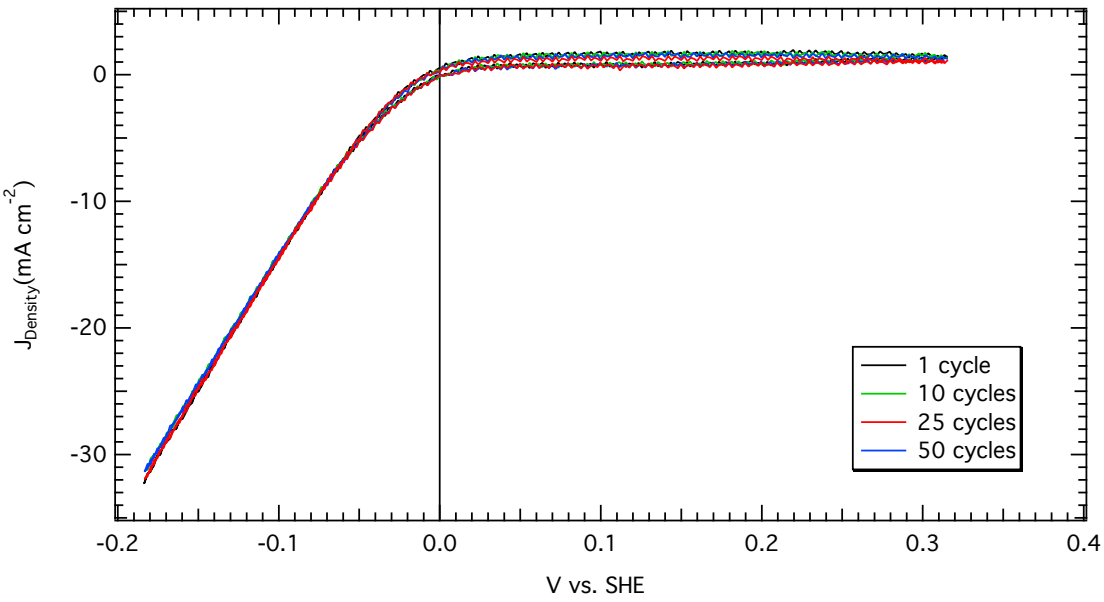

Figure 19: Cyclic Voltammogram of a thin PtNP layer on ITO cycled at 50 mV s^{-1} and submerged in 0.5M H_2SO_4 with constant stirring.

After continuously sweeping the potential back and forth for 25 cycles, almost no discernable drop in current density is observed. Upon scanning an additional 25 cycles, the current decreases by approximately 1 mA cm^{-2} at an applied overpotential of -183 mV vs. SHE. From these repeated measurements it is clear that samples of PtNPs adsorbed on ITO are electrochemically stable at low overpotentials on this time scale. However, at

high overpotentials, the voltage load on the electrode is greater and more current is driven through the catalyst. As a consequence, surface degradation may occur. In Figure 20, the CV experiment is repeated for another ITO/PtNP (identical catalyst loading) electrode scanned to a higher overpotential.

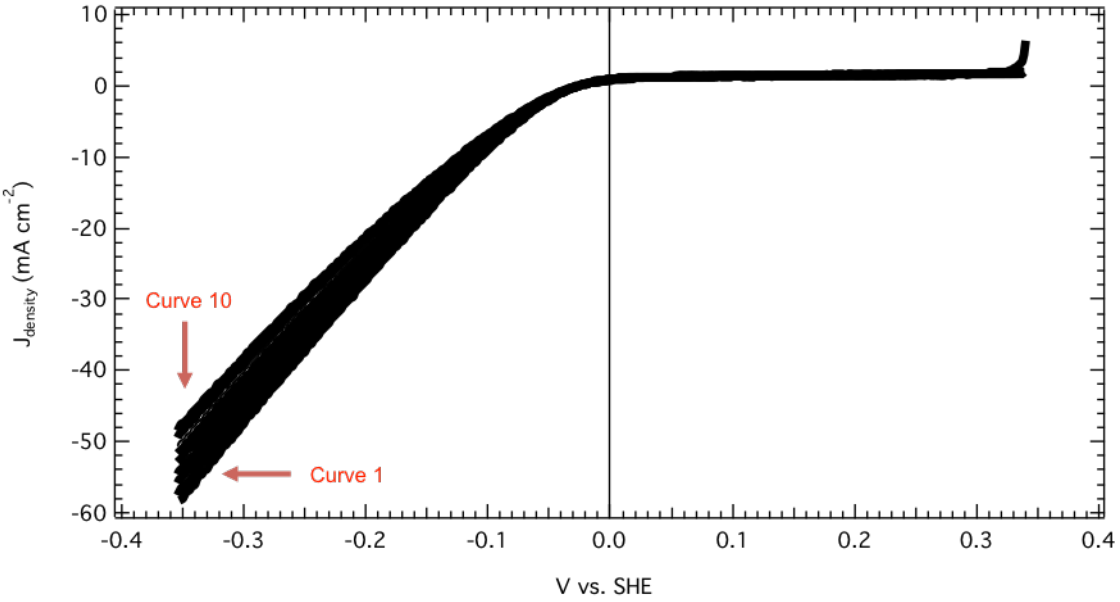

Figure 20. CV of PtNPs on ITO repeated for 10 cycles in 0.5M H_2SO_4 with constant stirring and a scan rate of 50 mV s^{-1}.

Figure 20 highlights an important occurrence at higher applied biases. The decrease in cathodic current is approximately 11 mA cm^{-2} after 10 cycles. As the PtNP sample is continuously swept to a high overpotential (-350 mV vs. SHE) there is a buildup of reaction products on the surface of the electrode. Qualitatively, small H_2 bubbles can be seen adhering to the electrode after several CV scans. Even with vigorous solution stirring, the bubbles do not readily discharge from the surface. This blockage prevents diffusion of new reactant species to the catalyst surface and leads to the

observed decrease in current density. Because slight electrode degradation may also contribute to the observed drop in current, chronoamperometry was employed to study current production over time. The chronoamperometry experiment (Figure 21) was performed at a fixed low overpotential, thus preventing considerable buildup of H_2 at the electrode interface.

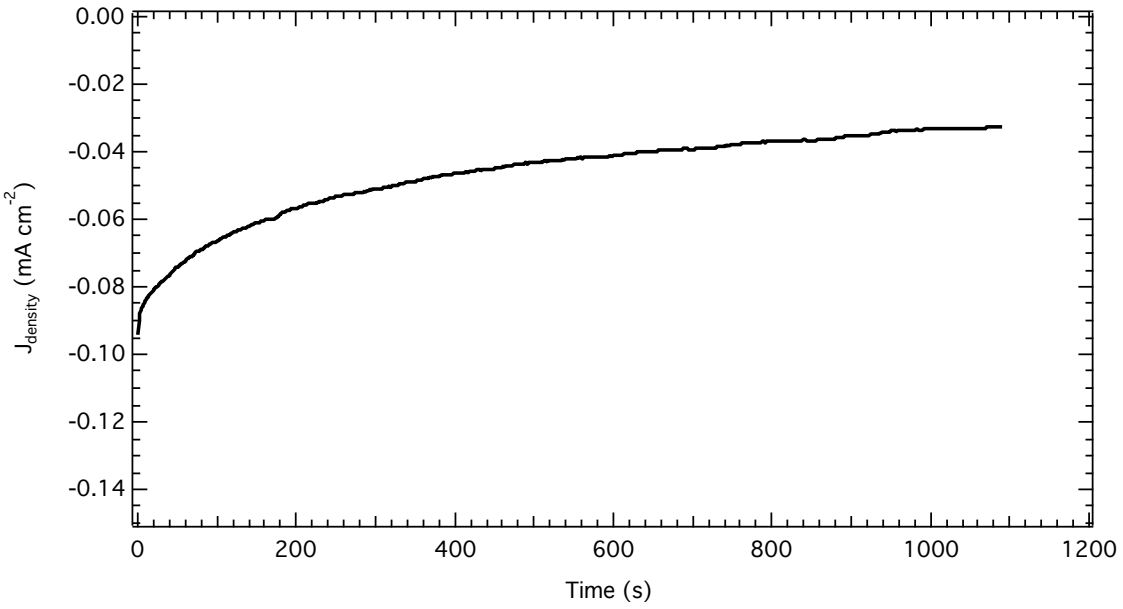

Figure 21: Chronoamperometry scan of ITO/PtNPs at an applied short circuit potential of 0.0 vs. SHE (-226 mV vs. Ag/AgCl ref.).

At almost no applied overpotential, the current density is much lower (40-100 μA cm^{-2} and the electrode surface appears free of bubbles. At the beginning of the measurement, current density production is the highest (approximately 94 μA cm^{-2} at 1 s) but begins to decrease over time. The current density is effectively halved (47 μA cm^{-2}) at 400 seconds but seems to plateau around 35 μA cm^{-2} after 1000 seconds. Because the current reduction over time is small (approximately 60 μA cm^{-2} over 1000 s), electrode

degradation in solution does not appear to be responsible for the substantial current reduction (approximately 11 mA cm^{-2} after 10 cycles) present in the cyclic voltammogram (Figure 20).

Increasing the ratio of catalyst present to the effective electrode surface area should also have an effect on HER activity. By adding larger mass loads, more catalyst surface area is exposed to solution and current generation increases (Figure 22).

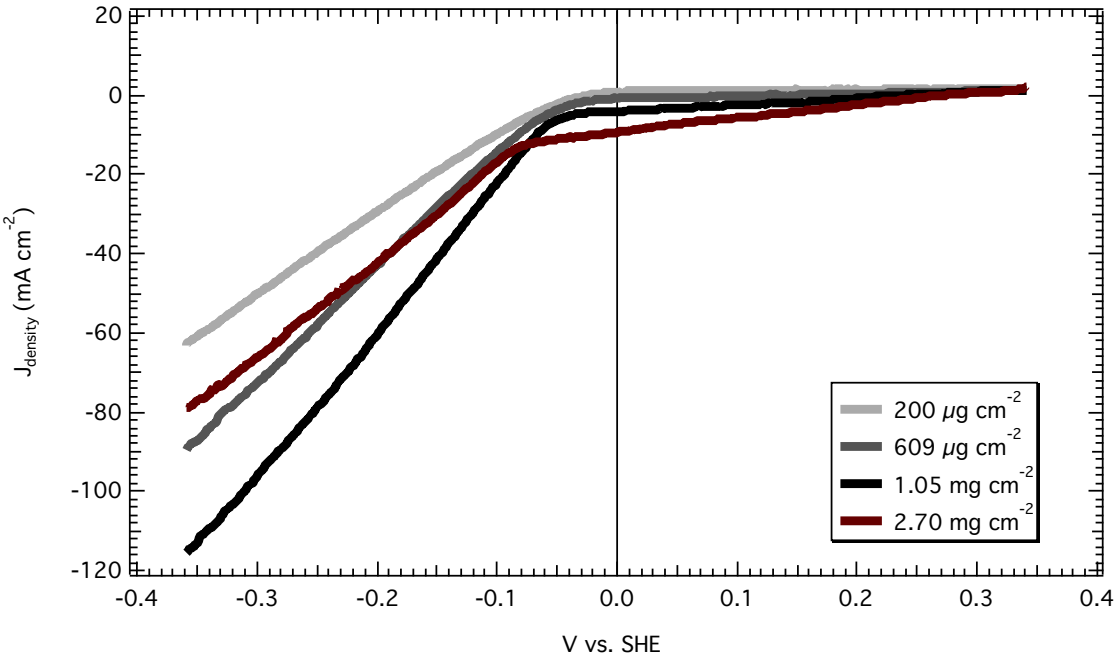

Figure 22: Linear sweep voltammogram for ITO/PtNPs with increasing mass loadings of platinum catalyst.

When more platinum particles are deposited on the ITO surface, a pronounced increase in current density occurs. At a mass loading of 1.05 mg cm^{-2}, the current density is the highest (118 mA cm^{-2} at -360 mV vs. SHE). This can be attributed to the higher surface area that occurs when more particles are added to the catalyst layer. However, with a higher PtNP load of 2.70 mg cm^{-2} (Figure 22, red line), the trend breaks down and

a large drop in current density occurs (78 mA cm^{-2} at -360 mV vs. SHE). This presents a clear limit to the improvements afforded by increasing the total catalyst surface area. Calculations of the projected surface area (surface coverage by the nanoparticles) allow us to estimate the number of stacked catalyst layers. Table 1 shows the calculated projected surface areas (PSA) of the PtNP samples in Figure 22 compared to the measured substrate surface area (SSA).

Table 1: Calculated projected surface area of PtNPs with different mass deposition loadings from Figure 22. A Platinum density of 21.45 g cm^{-3} and average particle diameter of 3 nm are assumed.

Mass load	Number of Particles	PSA (cm^2)	SSA (cm^2)	PSA:SSA
200 µg	6.59×10^{14}	46.6	0.344	136:1
609 µg	2.01×10^{15}	142	0.279	509:1
1.05 mg	3.46×10^{15}	245	0.321	762:1
2.70 mg	8.90×10^{15}	629	0.440	1430:1

When more material is stacked on the ITO substrate, the PSA of the catalyst increases drastically but does not scale directly with the experimentally obtained current densities in Figure 22. That is to say, the 609 µg sample possess roughly three times the projected catalyst surface area as the 200 µg test but the current density is only greater by a factor of about 1.5 (90 vs. 60 mA cm^{-2} at -360 mV vs. SHE) from Figure 22. A distinct difference in projected surface area and electrochemically active surface area (ECSA) exists. Several factors may contribute to this discrepancy. First, particle packing (touching) results in a small reduction in the true surface area of the spherical particles. Ligand coverage on the PtNPs plays a larger role, further restricting the available surface area. Besides these two points, diffusion and conductivity challenges are most likely the major causes of the inconsistency between catalyst surface area and ECSA at high mass

loadings. Even for a relatively thin PtNP film (200 μg), the ratio of projected surface area to substrate surface area (PSA:SSA) is quite large (136:1). A PSA:SSA ratio of 1:1 would indicate a PtNP monolayer of surface coverage. This means even a small mass deposition of 200 μg PtNPs covers the substrate area many times over. When the PtNP mass is increased to 2.70 mg, the total projected catalyst area increases to 629 cm^2 and the PSA:SSA ratio is huge (1430:1), but the ECSA clearly does not increase comparably, as evidenced by the JV curve. The high PSA:SSA ratio indicates a massive number of catalyst layers which must be responsible for the noted decrease in current density. Because the catalyst film is so thick, diffusion of reactants is severely hindered and the underlying layers are inaccessible. This leads to a much lower ECSA as only the electrically connected top levels are active. However, if diffusion of species into the high surface area electrode is the primary limiter of current density, then at high catalyst mass loadings (many layers), tests should plateau around the same current values. This is not the case as the 2.70 mg cm^{-2} sample in Figure 22 performed far worse than the 1.05 mg cm^{-2} and 609 μg cm^{-2} loaded electrodes.

The conductivity of these films must also factor in. Unlike in the bulk metal, the Pt atoms in adjacent nanoparticles do not touch directly, and are separated by an encapsulating overlayer of ligands. This must result in an intrinsic electrical resistance that increases with catalyst layer thickness. When high amounts of PtNPs are present (2.70 mg cm^{-2}), electrical contact between the top layers at the solution interface and the conductive substrate is impeded. This limits the electrochemically active surface area of the catalyst and gives rise to the decrease in current density in Figure 22.

3.3 Surfactant Removal for Surface Cleaning

When the catalyst layer is sufficiently thin (~250 μg cm^{-2}), the effects of diffusion and film conductivity on performance are reduced. At this scale, the surfactant overlayer on the NP surface dominates in blocking surface reaction sites. For solution-based synthesis, ligands are needed as capping agents for metal nanoparticle growth and to maintain dispersibility. While these surfactants offer control over size and shape during nanocrystal formation (important parameters when designing a catalyst), their presence ultimately limits efficiency by directly blocking surface reaction sites. Low-temperature thermal annealing has previously been successful in surfactant removal from platinum nanoparticles without inducing significant surface perturbations.[49] In accordance with this work, total ligand removal is essential to improving the reactivity of our metal catalyst. Several surfactant removal methods are outlined in Figure 23.

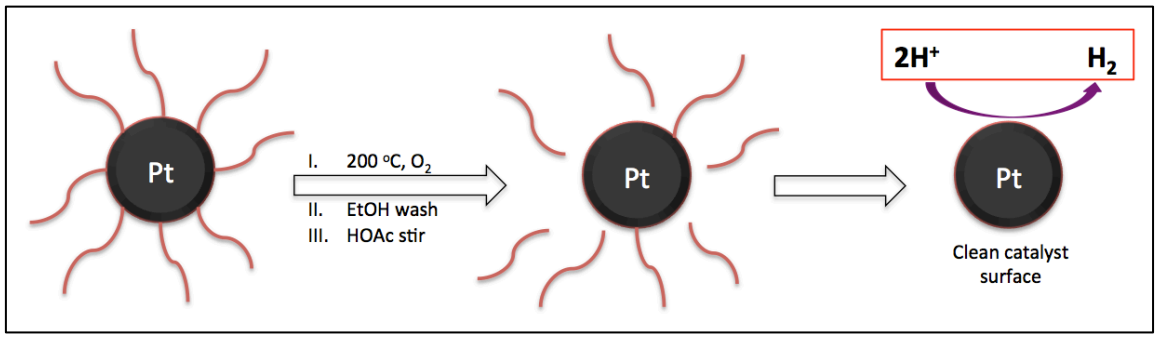

Figure 23: Techniques for removing ligands from untreated PtNPs in order to expose more surface area.

Additionally, cleaning the nanoparticle surface should decrease distance between particles, improve contact and further enhance conductivity. The results of these physical and chemical treatments are presented in the following sections.

3.3.1 Heat treatment

To investigate the possibility of thermal processing as a route for significant ligand removal, thermogravimetric analysis (TGA) was first performed on a dry sample of PtNPs (Figure 24). Table 2 shows selected mass loss percentages at several temperatures.

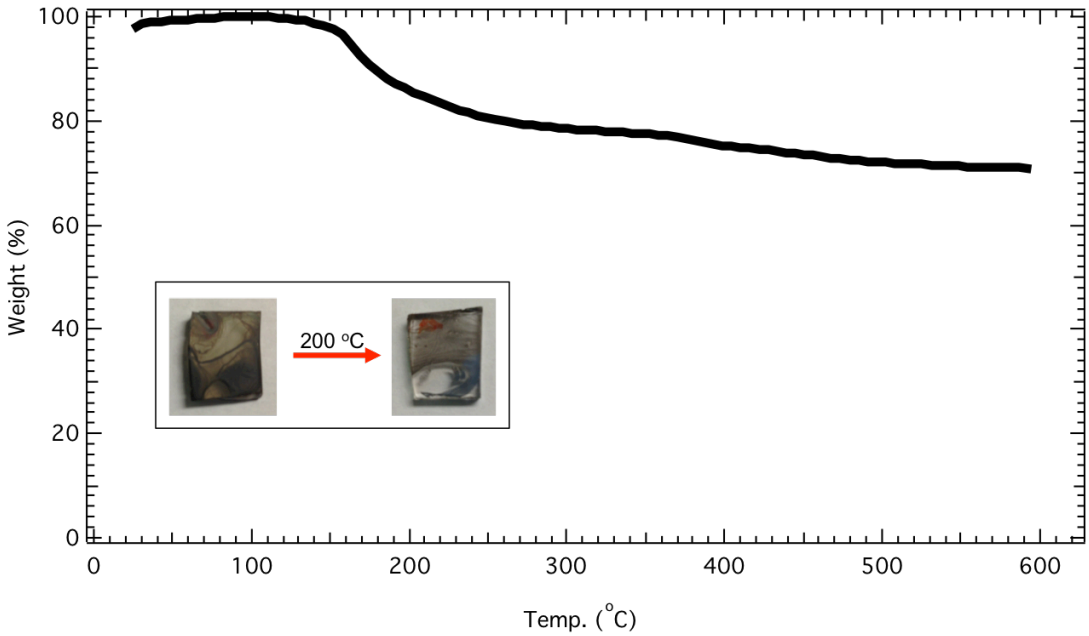

Figure 24. TGA of dry untreated PtNP sample. The inset images show a visible change in appearance upon heating for two similar films of PtNPs on glass.

Table 2: Percentage mass loss from total for the same dry PtNP sample across a temperature range of 150-600 °C.

Temperature (°C)	Mass loss (%)
150	2.5
180	10.6
200	14.1
300	21.5
400	24.9
600	29.2

Here, the TGA profile indicates a noticeable mass loss of 2.5% after heating to 150 ^{o}C in air. A more significant loss of 14.1% is observed when the PtNP sample is further heated to 200 ^{o}C. This change in sample weight can be attributed to the thermal removal of bound oleic acid and oleylamine ligands. At much higher temperatures (400-600 ^{o}C), small changes in mass are observed (24.9-29.2% loss). To qualitatively examine these heat effects, a sample of adsorbed untreated PtNPs (~10 mg) on glass was heated in air (Figure 24, inset). After heating to approximately 180 ^{o}C (mass loss of 10.6%, as indicated by Table 2), the initial black color of the deposited particle layer undergoes a noticeable change, producing a more metallic-looking surface. Because P3HT:PCBM BHJ blends typically require annealing at temperatures around 180 ^{o}C but not greater than 200 ^{o}C, we chose not to pursue higher processing temperatures for our heat treatment studies.[18] Noble metals like platinum are exceptionally resistant to corrosion and do not readily form substantial native oxide layers in air. Nevertheless, platinum oxide formation has been found to not affect or limit catalysis on the nanoparticle surface.[55]

TEM images confirm no drastic morphological change occurs on the nanoparticle surface after it is subjected to high temperatures (Figure 25).

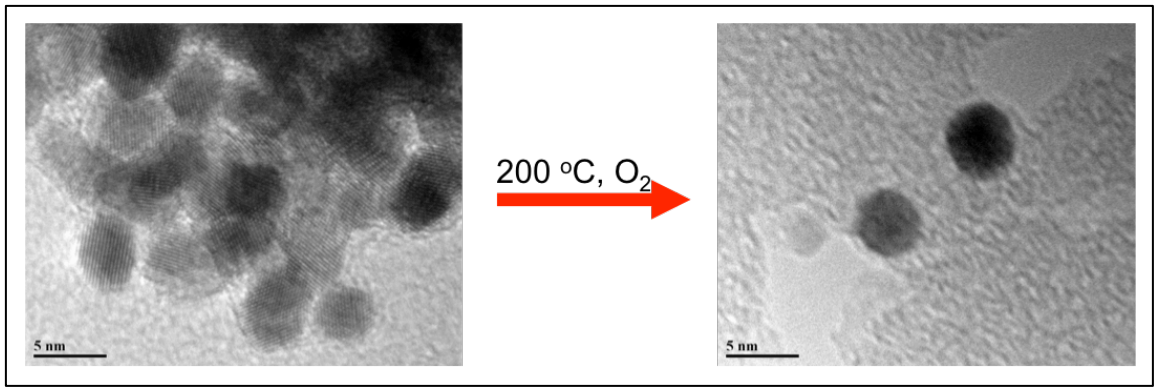

Figure 25. TEM image of PtNPs before and after heating to 200 °C. The image on the right shows clear distortion of the carbon mesh support but intact nanoparticles. The scale is 5 nm.

Relevant electrochemistry was then performed to determine the effects of heat treatment at several temperatures on the JV characteristics of the platinum catalyst. Several ITO electrodes were created with identical mass loadings (250 µg) of PtNPs. Two of the samples were then heated in a furnace at 150 and 200 °C. Figures 26 and 27 show the JV response and Tafel plots for heated and room temperature films of PtNPs on ITO.

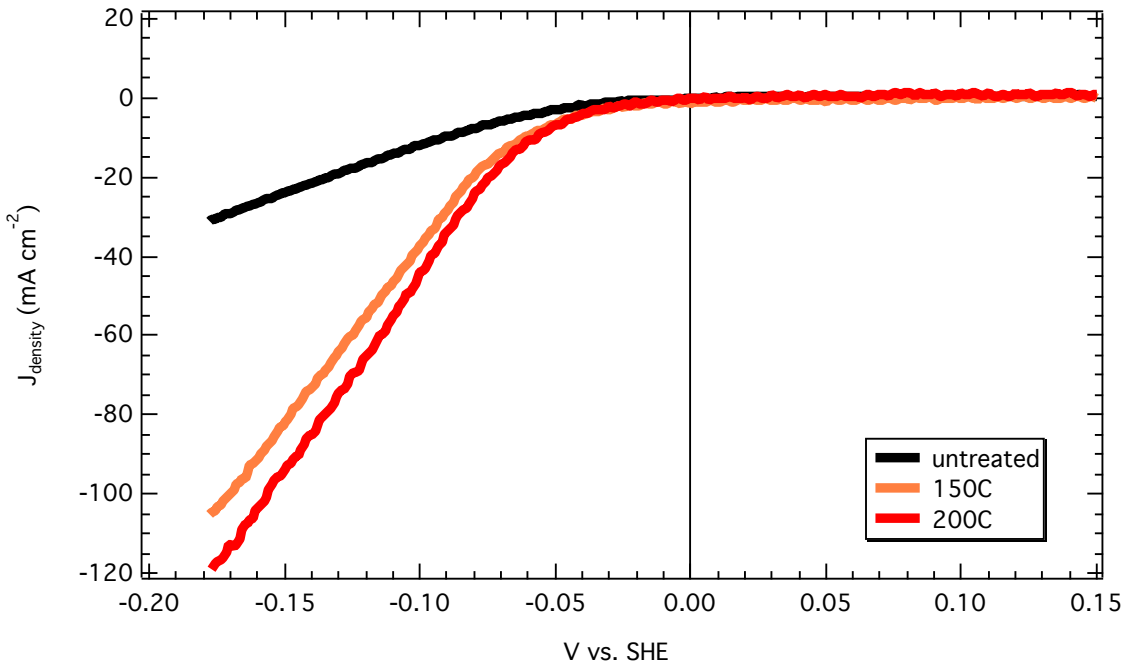

Figure 26: Linear sweep voltammogram for several heated ITO/PtNPs samples in 0.5 M H_2SO_4 with constant H_2 bubbling and vigorous stirring.

In the figure above, the effects of heating the PtNPs are unmistakable. The three catalysts in this series demonstrate HER activity at comparable overpotentials (-0.060 mV vs. SHE) to achieve current densities greater than 10 mA cm^{-2}. However, the effects at greater overpotentials are even more pronounced. At an applied overpotential of -0.178 mV vs. SHE, the untreated PtNPs produce a catalytic current density of just 32 mA cm^{-2}, compared to approximately 105 mA cm^{-2} and 120 mA cm^{-2} for the PtNPs heated at 150 and 200 ^{o}C. This large increase in catalytic current density is attributed to the thermal removal of bound ligands that occurs after heating at high temperatures.

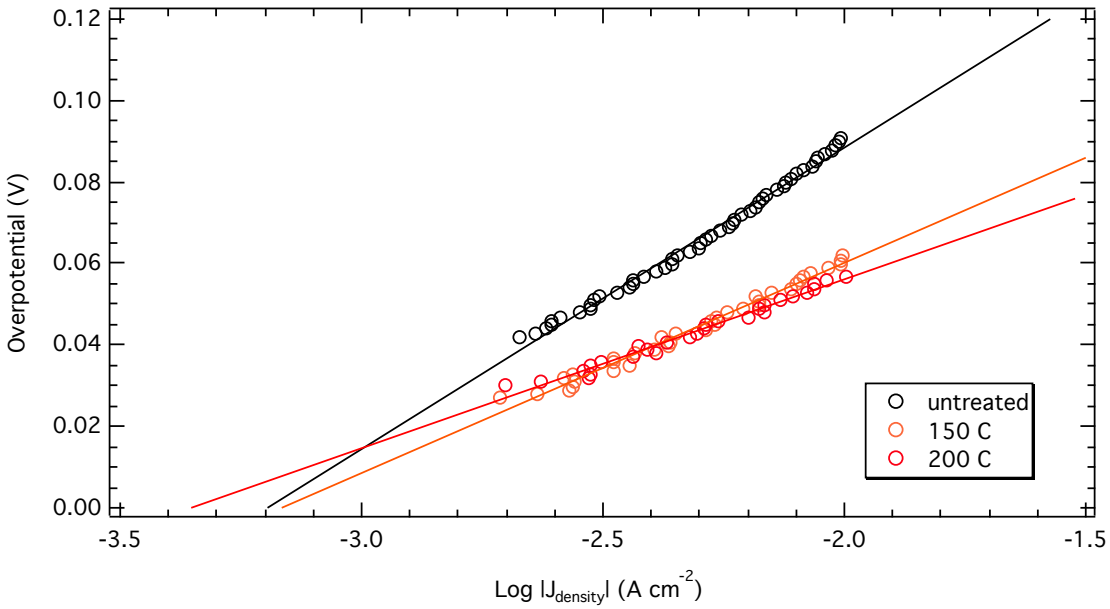

Figure 27: Tafel plots constructed for the same thermally treated PtNP series. Thin lines represent extrapolations of the linear regions used to calculate the exchange current density, J_0.

The Tafel plots provide valuable information about the catalyst surface at the start of the hydrogen evolution reaction (i.e. at low overpotentials). Important parameters of the Tafel relation are tabulated below. Standard errors in b and J_0 were calculated at 95% confidence.

Table 3: Summarized Tafel data for heat treated PtNPs including the important parameters b (Tafel slope) and J_0 (exchange current density).

Platinum Species	Tafel slope, b (mV dec^{-1})	Exchange current, J_0 (log [A cm^{-2}])
untreated PtNPs	74.1 ± 1.0	-3.194 ± 0.002
150 ^{o}C	51.7 ± 1.0	-3.166 ± 0.002
200 ^{o}C	41.5 ± 1.1	-3.354 ± 0.003
Pt metal	30.0[56]	-3.1 [(57)]

From the Tafel plot, extrapolation of the linear portion to the x-axis gives the exchange current density, J_0, at theoretical zero overpotential. J_0 depends integrally on the surface nature of the metal. Factors that affect surface structure (passivating oxides, surface roughness, adsorbed species) will change the hydrogen adsorption free energy and be reflected in the value of J_0. For smooth platinum, this value is quite low, normally reported around -3.1 log [A cm^{-2}] or 7.94 x 10^{-4} A cm^{-2}.[57] The exchange current densities are similar for the nanoparticle series (-3.194 log [A cm^{-2}] for untreated and -3.354 log [A cm^{-2}] for PtNPs annealed at 200 ^{o}C), which is expected because they are still platinum so intrinsic properties such as activation energy of hydrogen adsorption, are largely unchanged.

Perhaps more important is the Tafel slope, *b*, which can be used to determine the rate-limiting step for the mechanism of hydrogen evolution. As discussed in section 1.5, the mechanism can be broken down into three elementary steps- the initial discharge (Volmer) followed by either an electrochemical desorption (Heyrovsky) or atomic hydrogen combination (Tafel) step. At low overpotentials, the value of the Tafel slope is indicative of the rate-determining step and should be around 120, 40, or 30 mV dec^{-1}, respectively.[41,58] When the discharge reaction is fast and the H_{ads}-H_{ads} combination step is rate-limiting, the Tafel slope has been derived to be 2.3RT/2F or 0.029 V dec^{-1} at 25 ^{o}C.[58] Experimentally, this value is well established on bulk platinum with typical values around 30.0 mV dec^{-1}.[56] While the untreated PtNPs exhibit a Tafel slope that suggests a mechanism somewhere between the Vollmer-Heyrovsky steps, the slope notably decreases following thermal processing. The higher Tafel slope of the untreated PtNPs appears to arise from ligand coverage on the catalyst that slows the initial discharge and

adsorption of protons to the surface. The Tafel slope for the 150 ^{o}C treated nanoparticles was 51.7 ± 1.0 mV dec^{-1}. The slope decreased to 41.5 ± 1.1 mV dec^{-1} when the processing temperature was increased to 200 ^{o}C. This indicates that the heat treated PtNPs proceed via the Volmer-Heyrovsky mechanism and the electrochemical desorption (Heyrovsky reaction) is rate-limiting. The decrease in Tafel slope behavior can therefore be attributed to cleaning of the catalyst surface. A small slope further corroborates the current boosting effects of heat processing the nanoparticle catalyst because it shows significant improvement in catalytic current density occurs with only a moderate increase in overpotential. Recently, it has been reported that heat treatment may induce a slight rearrangement of surface atoms on the platinum nanoparticles that may contribute to changes in J_0 and b.[55]

3.3.2 EtOH Wash and Centrifugation

To assess the viability of chemical washing as another means of surfactant removal, a portion of PtNPs were cleaned by successive washes in ethanol (EtOH) and compared to the original reaction mixture (designated again as untreated PtNPs). Infrared (IR) Spectroscopy (Figure 28) was first preformed to evaluate the degree of oleic acid and oleylamine ligand elimination after many washes.

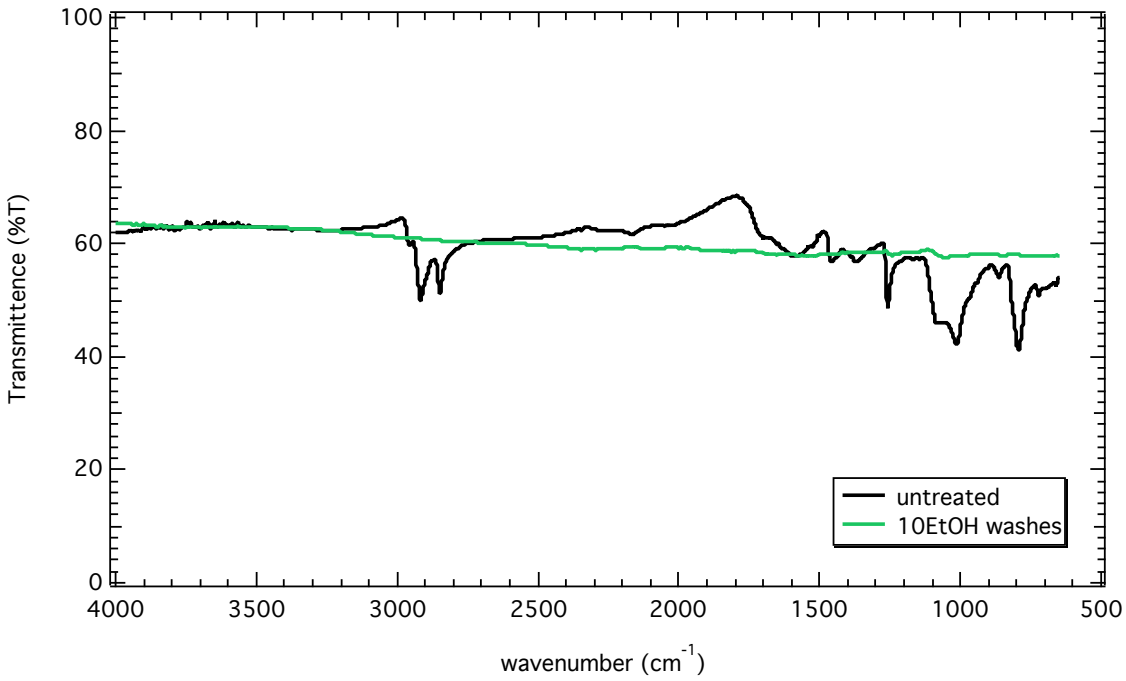

Figure 28: FT-IR spectra for untreated (black) PtNPs and PtNPs after 10 successive washes with ethanol (green). Samples were dried under vacuum prior to the analysis.

The observed stretches at 2850 cm^{-1} and 2950 cm^{-1} in the untreated (black line) PtNPs are representative of the C-H vibrations in oleylamine molecules.[59] These bands disappear after 10 rinse and centrifugation steps, suggesting successful elimination of bound ligands. TEM images (Figure 29) of the washed PtNPs verify that no significant changes occur to nanoparticle morphology due to the chemical washing process.

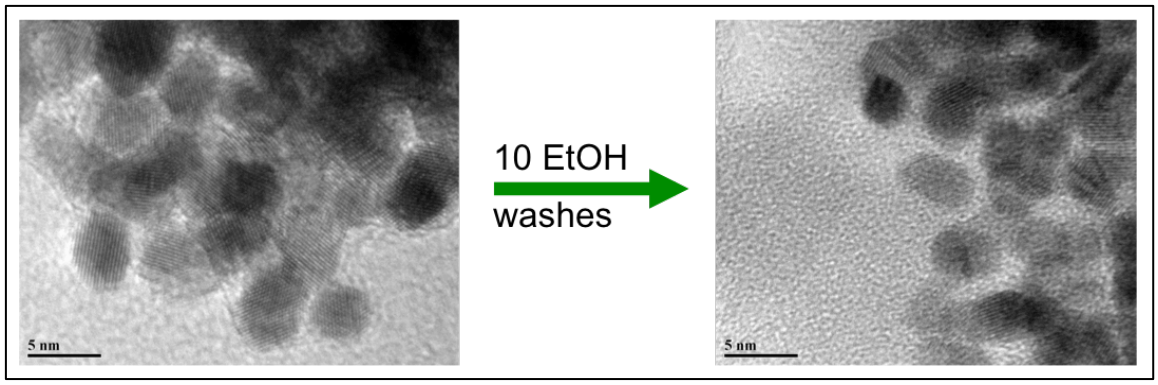

Figure 29. TEM images of the same PtNP sample before and after 10 washes with ethanol. The scale bar is 5 nm.

Samples of untreated and washed nanoparticles were then deposited on ITO and their JV characteristics were measured with linear sweep voltammetry (Figure 30, below). Because the catalytic current also increases with the amount of catalyst, each electrode had a controlled mass loading of 250 μg cm^{-2}.

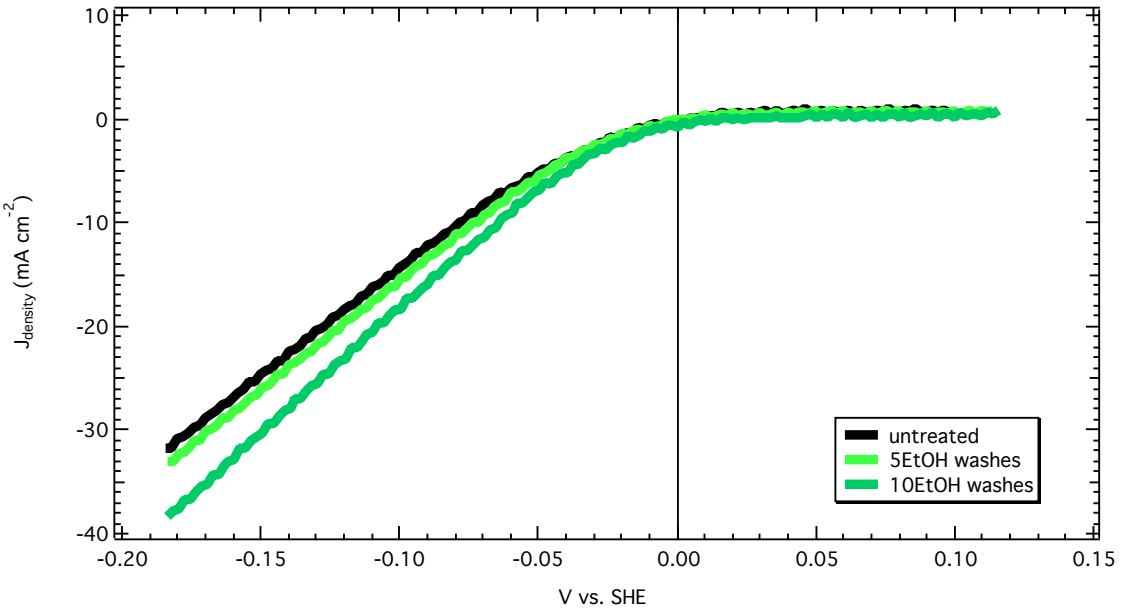

Figure 30: Linear sweep voltammograms for the ethanol washed PtNPs series deposited on ITO. Measured in H_2-saturated 0.5M H_2SO_4 with constant stirring.

After considerable washes, an increase in catalytic current is observed. To produce a current density of 10 mA cm^{-2}, an overpotential of just -0.064 V vs. SHE was applied to the ITO/PtNP electrode that had been washed 10 successive times with ethanol. In comparison, a higher overpotential of -0.080 V vs. SHE was required to produce the same current density on the unwashed sample. At considerably higher overpotentials, the growth in current density is even more pronounced in the treated platinum sample. Tafel plots were then constructed from the transformed JV data.

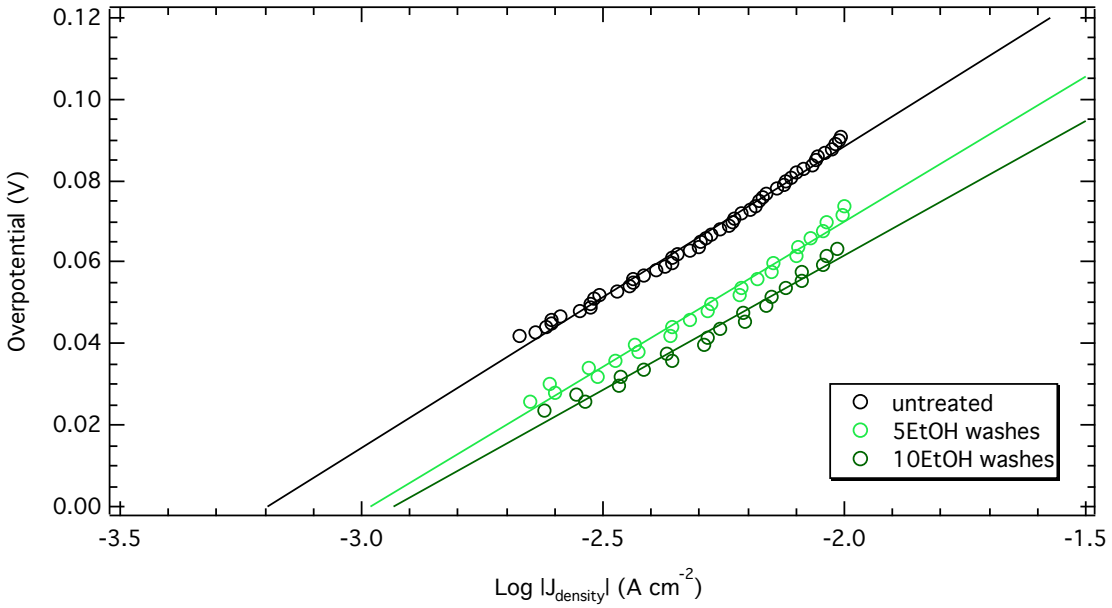

Figure 31: Tafel plots for the ethanol washed PtNP series. Thin lines represent extrapolations of the linear regions used to calculate the exchange current density, J_0.

The important Tafel parameters (b, J_0) are summarized in the following table with standard errors reported at 95% confidence. Literature values for smooth Pt metal are also included for comparison.

Table 4: Tabulated Tafel data for PtNPs washed multiple times with ethanol. The important parameters *b* (Tafel slope) and J_0 (exchange current density) are included.

Platinum Species	Tafel slope, *b* (mV dec^{-1})	Exchange current, J_0 (log [A cm^{-2}])
untreated PtNPs	74.1 ± 1.0	-3.194 ± 0.002
5EtOH washes	71.4 ± 1.9	-2.980 ± 0.004
10EtOH washes	66.0 ± 2.1	-2.912 ± 0.005
Pt metal	30.0[56]	-3.1 [(57)]

As with the heat-treated variety, the PtNPs washed with ethanol demonstrate exchange current densities (-2.980 log [A cm^{-2}] after 5 washes and -2.912 log [A cm^{-2}] after 10 washes), indicating the hydrogen adsorption free energy is comparable to bulk platinum.

After rinsing 10 times with ethanol, the Tafel slope decreases from 74.1 ± 1.0 mV dec^{-1} to 66.0 ± 2.1 mV dec^{-1}. As previously mentioned, the reduced slope indicates that small changes in overpotential give pronounced increases in current density. However, neither of the *b* values (71.4 mV dec^{-1} and 66.0 mV dec^{-1}) for the washed PtNPs closely match those predicted by the Volmer (120), Heyrovsky (40) and Tafel (30) reactions. As a result, the exact rate-limiting step cannot be determined and the mechanism of hydrogen evolution appears to proceeds by some combination of these steps. Most likely, some small amount of bound surfactants or leftover wash residue still present on the catalyst surface and is responsible for the slow initial discharge step that prevents true Heyrovsky or Tafel behavior.

3.3.3 Stir in Acetic Acid

Finally, a second chemical washing technique was pursued to clean the platinum nanoparticle surface and improve HER activity. For this study, a portion of PtNPs straight from the reaction mixture (untreated) was vigorously stirred in glacial acetic acid

(HOAc) for up to 24 hours. As with the ethanol washed variety, IR Spectroscopy (Figure 32) was employed on the final clean, dry particles to investigate the level of oleylamine and oleic acid ligand removal.

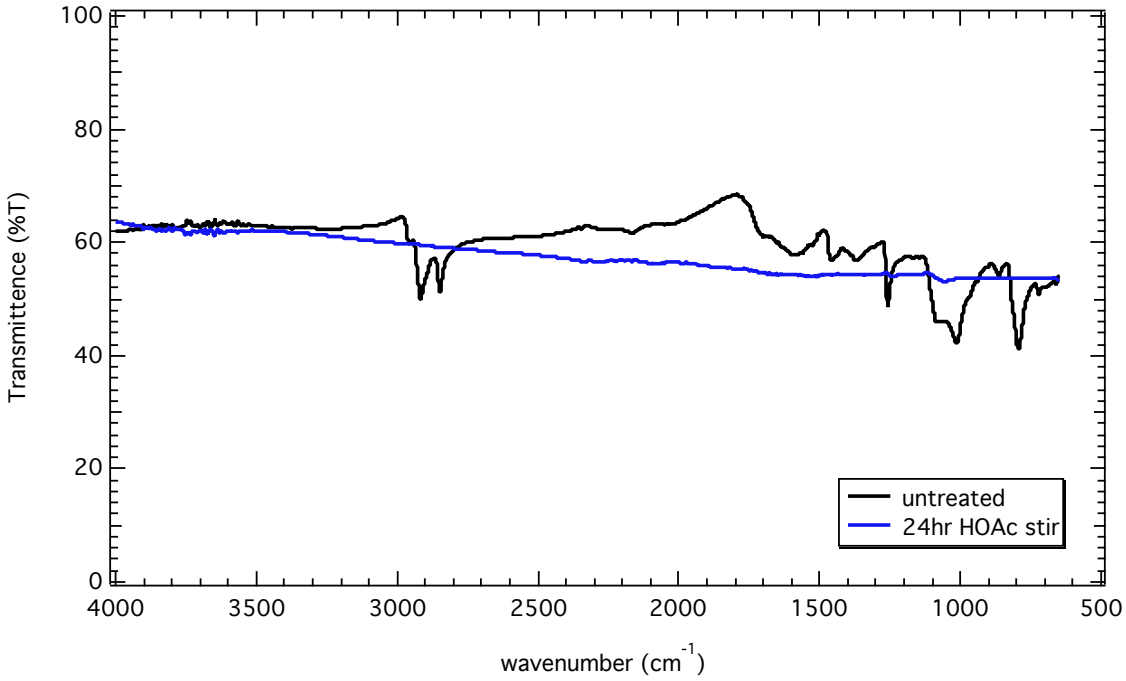

Figure 32: FT-IR spectra for untreated (black) PtNPs and PtNPs after stirring for 24 h in glacial acetic acid (blue). Samples were dried under vacuum prior to the analysis.

Once again, the IR spectra shows a loss of C-H stretches at 2850 cm^{-1} and 2950 cm^{-1} after the PtNPs are stirred for 24 hours in acetic acid. Additionally, TEM (Figure 33) was performed to characterize the washed particles and ensure the surface morphology remained unchanged.

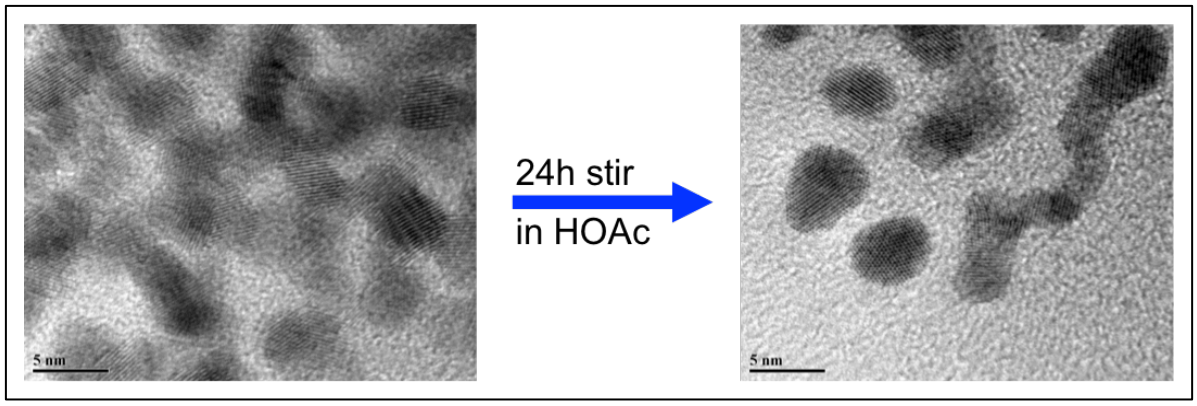

Figure 33: TEM images of dry PtNPs as synthesized and after stirring in acetic acid.

In accordance with previously prepared electrodes, equal amounts of treated and untreated catalyst were deposited on ITO to give identical loading masses of 250 µg per unit area. LSV was then performed on fabricated ITO/PtNPs electrodes to study their JV characteristics, as shown in Figure 34.

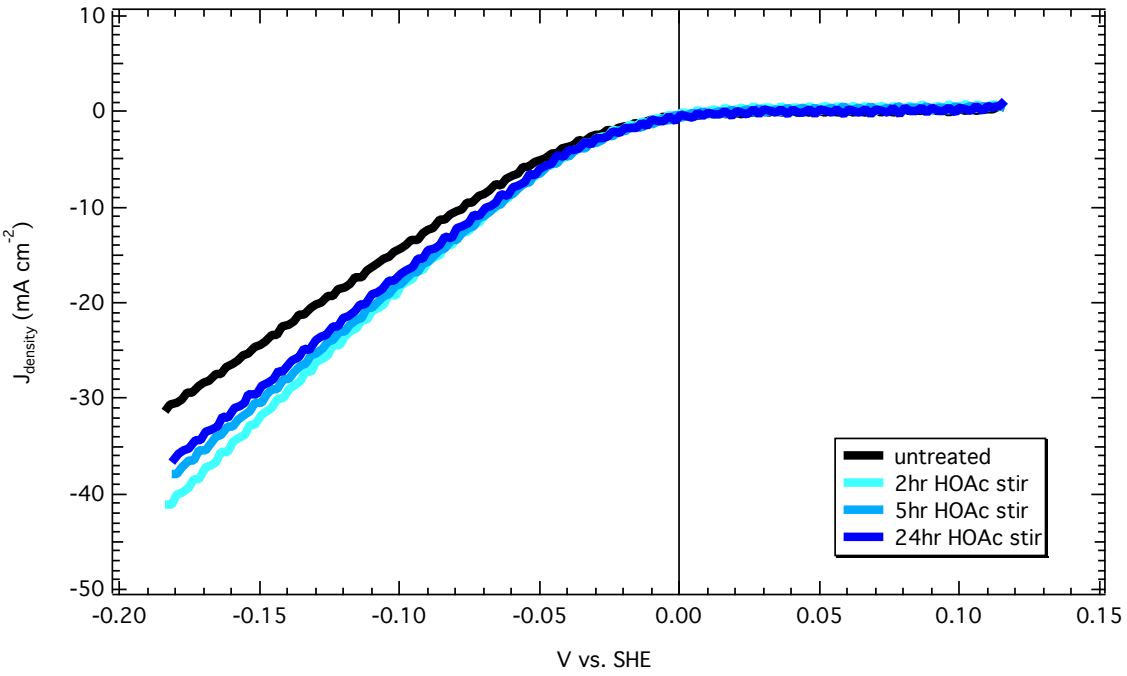

Figure 34: Linear sweep voltammograms for PtNP samples deposited on ITO after stirring in acetic acid. Measured in H_2-saturated 0.5M H_2SO_4 with constant stirring.

After stirring for 2 hours in acetic acid, the PtNP electrode performed superiorly, achieving a 10 mA cm^{-2} current density at -0.065 V vs. SHE, compared to -0.080 V vs. SHE for the untreated variety. However, devices fabricated from PtNPs that had stirred for longer periods (5 and 24 hours) performed worse (-0.067 and -0.071 V vs. SHE for current densities of 10 mA cm^{-2}), albeit still better than the untreated particles. Constructing Tafel plots may help elucidate this occurrence.

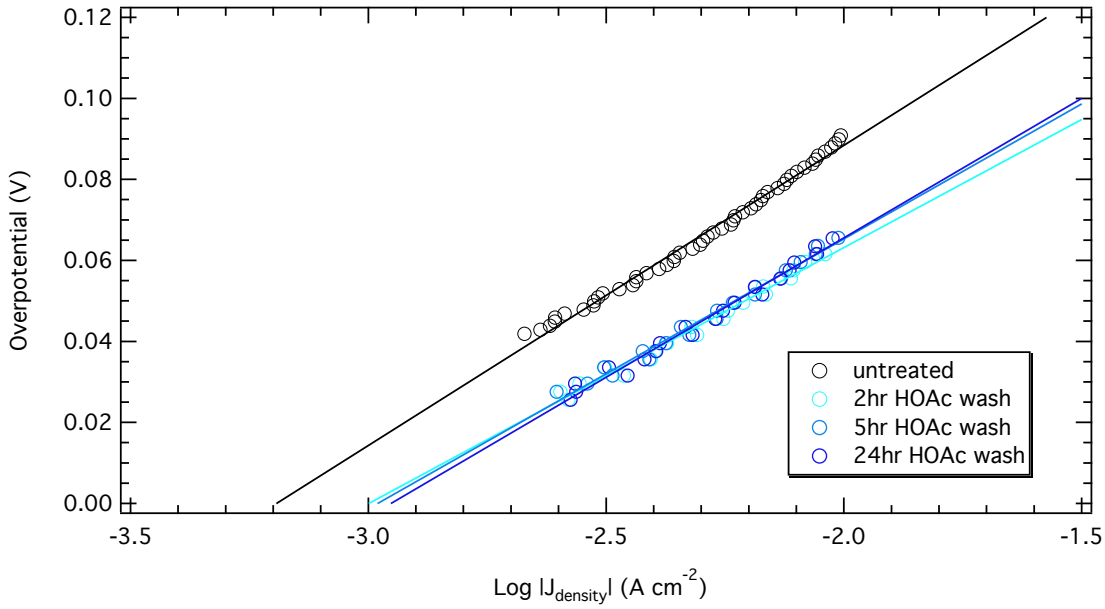

Figure 35: Tafel plots of the transformed JV data for the PtNP series washed in acetic acid. Thin lines represent extrapolations of the linear regions used to calculate the exchange current density, J_0.

Table 5: Comparison of Tafel parameters (slope and exchange current density) for PtNPs after stirring in glacial acetic acid (HOAc).

Platinum Species	Tafel slope, *b* (mV dec^{-1})	Current density, J_0 (log [A cm^{-2}])
untreated PtNPs	74.1 ± 1.0	-3.194 ± 0.002
2h HOAc wash	63.2 ± 1.9	-3.000 ± 0.005
5h HOAc wash	66.6 ± 1.8	-2.981 ± 0.004
24h HOAc wash	68.9 ± 1.9	-2.951 ± 0.004
Pt metal	30.0[56]	-3.1 [57]

The Tafel data (Table 5) shows a similar trend. Compared to the untreated PtNPs, the 2 h HOAc stirred sample demonstrates a J_0 value similar to smooth Pt (-3.000 ± 0.005 log[A cm^{-2}]) and a lower Tafel slope (63.2 ± 1.9 mV dec^{-1}). This coincides nicely with the JV data, confirming that the 2 h washed sample was the most active HER catalyst of the series. When the wash time is increased to 5 and 24 hours, the J_0 value does not change considerably (-2.981 ± 0.004 log [A cm^{-2}] at 5 h and -2.951 ± 0.004 log [A cm^{-2}] at 24 h). On the other hand, the Tafel slopes decreases to 66.6 ± 1.8 and 68.9 ± 1.9 mV dec^{-1}, meaning the mechanism of hydrogen evolution cannot be determined as some unknown species is responsible for slowing the initial H^+ discharge step to the catalyst surface. Initially, it was believed that some acetate groups may be exchanging with present surfactants (oleic acid and oleylamine) and binding to the nanoparticle surface during the stirring steps. However, the FT-IR spectra in Figure 32 shows no substantial C-H stretching, indicating this may either not be the case or acetate groups are present at extremely low concentrations. Nevertheless, the 5 and 24 h acetic acid treated PtNPs do still outperform the unwashed sample, suggesting ample ligand removal and improved HER catalytic ability.

Before concluding this section, it is important to mention several items pertinent to Tafel plot creation for the preceding data sets (heat treatment, ethanol rinse and acetic acid wash). First, the constructed graphs were obtained by plotting the absolute value of the overpotential (V vs. SHE) as a function of the $\log_{10}$ of the current density in A cm^{-2}. A linear regression analysis was performed on the linear portion of the curve (data points were removed until all regressions gave an $R^2 \geq 0.98$) at low overpotential to calculate values for b and J_0. Beyond the linear region, the current density begins to deviate from

the exponential Tafel behavior due to a combination of the diffusion limit of H^+ and blockage of the catalyst site by generated H_2 bubbles. Experimentally, the Tafel relationship has been shown to break down at high current densities on platinum.[56] This leads to large slopes at high overpotentials. Our studies validate this for our PtNPs, and only low overpotentials (below 100 mV vs. SHE) were used for these analyses.

3.4 JV Characteristics of a P3HT:PCBM BHJ Photocathode

3.4.1 Stability and Light Response

As addressed in section 1.4, P3HT:PCBM bulk heterojunction OPVs are incredibly well characterized in the literature with respect to blend ratio, film thickness, annealing temperatures and interfacial charge transfer characterisitcs.[17,20,23] However, submersion in acidic media under reducing electrochemical conditions offers a host of new challenges so that some old paradigms may need to be revisited. Photoactive P3HT films in water have been reported before but demonstrate extremely low photocurrent densities (about 0.5 μA at -0.500 V vs. SCE) as a result of inefficient charge extraction (i.e. no acceptor species) and injection into solution.[60] To our knowledge, there is one recent case of a P3HT:PCBM BHJ cell for hydrogen evolution, where an alternative molybdenum catalyst is used.[61] Both of these sources cite considerable difficulties when introducing these organic polymer films to an aqueous environment. Because device stability is vital to practical application, we first choose to study the stability of our P3HT:PCBM photoelectrode in solution.

P3HT photo-oxidation is well documented in OPVs; light and diffused oxygen will interact and disrupt π-conjugation leading to degradation of the film.[62,63] The pathway by which PCBM degrades is primarily morphological and related to crystallite

formation when subjected to high ambient temperatures for long periods. For our purposes, P3HT:PCBM films must be stable in concentrated acid (pH 0), under strong reducing conditions and for considerable periods of time in air. UV-visible spectroscopy is a simple and effective means to study photochemical degradation because any destroyed π-conjugation in the polymer backbone will be reflected as a loss of absorption. Figure 36 below contains the UV-Visible absorption profile for a representative thin P3HT:PCBM (1:1 by mass) film, before and after several electrochemical measurements.

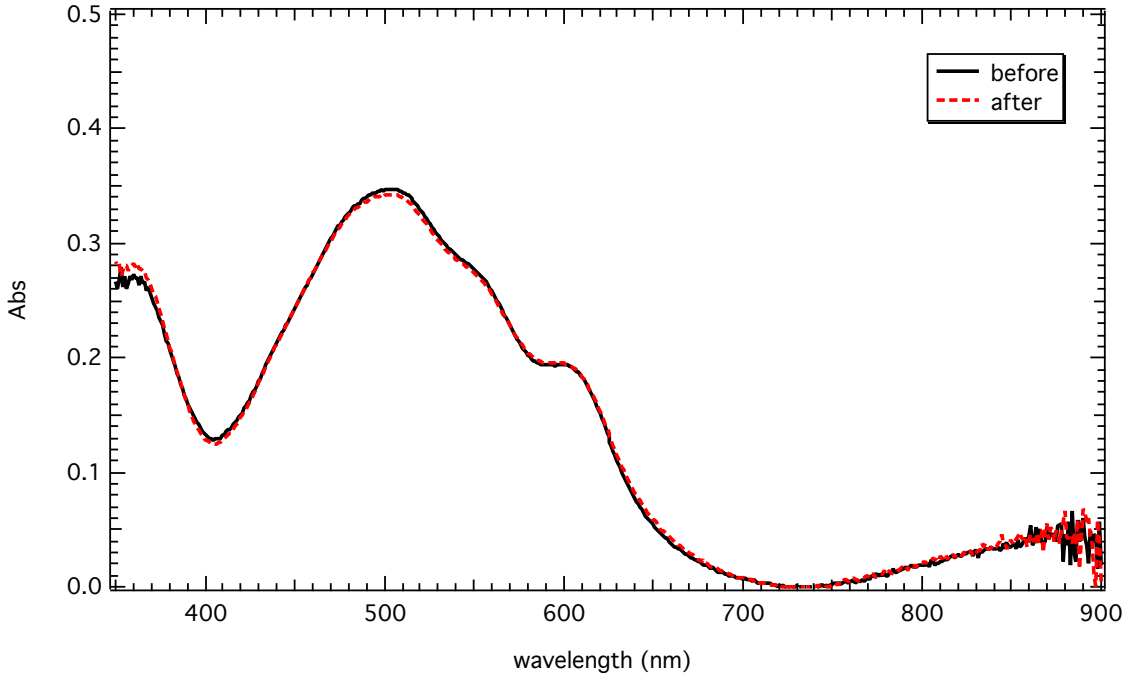

Figure 36: UV-Vis spectra of ITO/PEDOT:PSS/P3HT:PCBM before and after 10 CV cycles (dark and light) from +0.3 to -0.5 V vs. SHE at 50 mV s^{-1} in 0.5 M H_2SO_4.

The before and after absorption profiles show no drastic change occurs to the polymer film as a result of our tests. PCBM does not absorb in the visible region of the spectrum. Absorptions at red wavelengths (800-900 nm) are characteristic of oxidized

P3HT. This signifies that our polymer was partially oxidized to begin with and only slight oxidation may have occurred during electrochemical measurements.

To probe the effects of long-term light illumination on our photoelectrode, chronoamperometry (Figure 37) was employed on several devices constructed with different ratios of P3HT and PCBM. This also contributed valuable evidence concerning ideal blend ratio and PCBM stability.

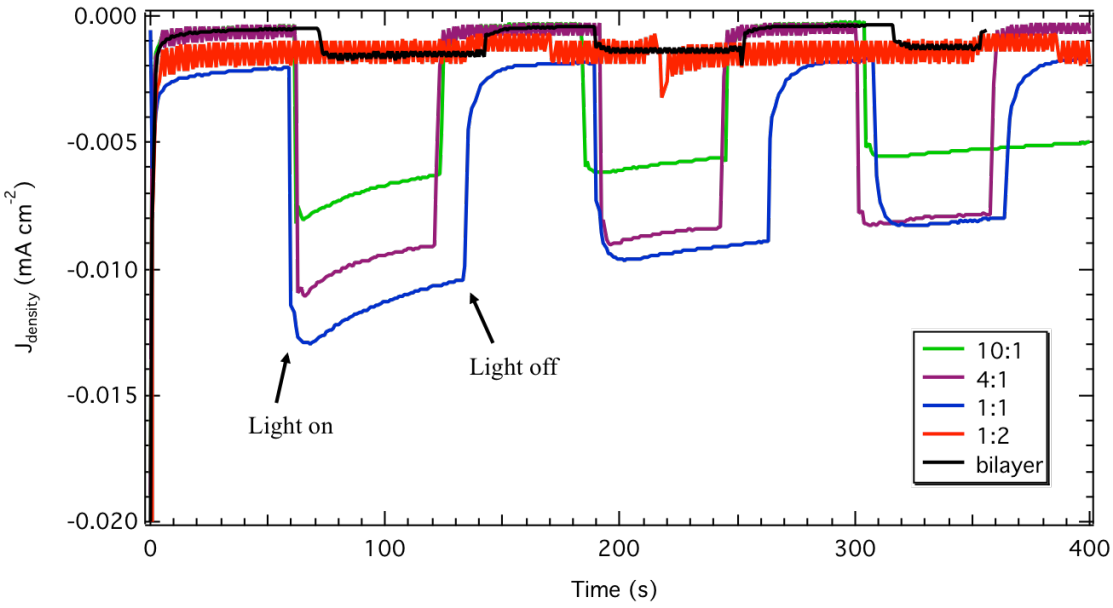

Figure 37: Chronoamperometry scan at short circuit potential (0 V vs. SHE) of several photoelectrodes with different mass ratios of P3HT:PCBM (see inset legend). Samles were illuminated with a power intensity of 100 mW cm^{-2} at AM 1.5 and submerged in 0.5M H_2SO_4.

Chronoamperometry studies are essential to evaluating photocurrent production over time. The scans above were measured at short circuit potential, i.e. the experimentally determined (H^+/H_2) redox potential. Once illuminated, an increase in observed current arises in almost every sample. Because electrons should only move

through the n-type semiconductor PCBM into solution, different blend ratios and a bilayer arrangement were investigated. However, the results show larger quantities of PCBM are actually detrimental; the 1:2 blend (red) and bilayer (black) device show almost no light response, despite being controlled to have the same amount of the P3HT absorber present. This degradation was observed qualitatively as these films quickly delaminated upon removal from solution. In contrast, the electrodes with more P3HT appeared nearly identical after chronoamperometry measurements, highlighting the importance of the polymer to prevent dissociation of PCBM into solution. For these films, photocurrent generation improves noticeably as the P3HT:PCBM ratio approaches a 1:1 blend. The 1:1 P3HT:PCBM achieves the highest initial current density (approximately 0.013 mA cm^{-2} at short circuit) but drops by several microamps after illumination for 60 s. This decrease in observed current over time occurs with the other devices in this series and seems to be independent of the blend ratio. Because P3HT does not appear to photodegrade in water, this current drop can be attributed to the build up of product species (molecular hydrogen) on the surface of the photoelectrode.

3.4.2 JV Characteristics of a Bare P3HT:PCBM Photocathode

Before addition of our platinum HER catalyst, the current-voltage characteristics of the bare P3HT:PCBM bulk heterojunction photocathode were measured by itself. The figure below shows the light and dark curve for a bare (no catalyst) 1:1 P3HT:PCBM film on ITO. The table that follows gives values for the open circuit potential (V_{oc}), short circuit current density (J_{sc}), maximum power point (P_{max}) as well as calculations of the fill factor (*ff*) and overall solar-to-hydrogen efficiency (η).

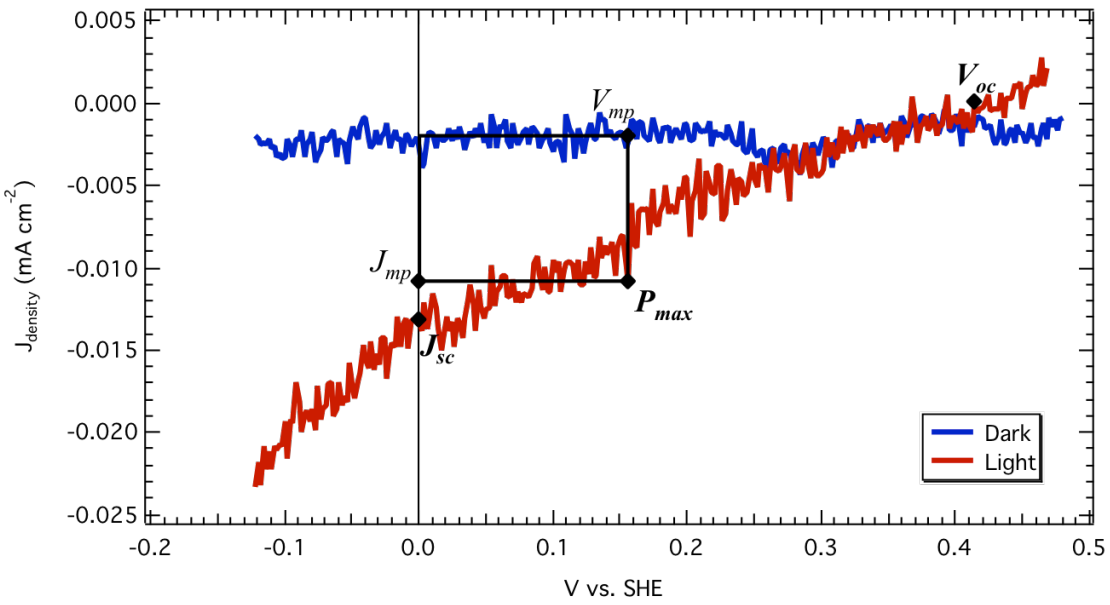

Figure 38: Dark (blue) and light (red) JV curves for an ITO/PEDOT:PSS/P3HT:PCBM electrode cycled at 50 mV s^{-1} in 0.5M H_2SO_4 under 100 mW cm^{-2} illumination at AM1.5.

Table 6: Tabulated data of important electrochemical parameters and calculations of fill factor (*ff*) and device efficiency (η).

V_{oc} (mV)	J_{sc} (mA cm^{-2})	P_{max} (mW cm^{-2})	*ff*	η (%)
414	0.013	1.56	0.289	0.016

When no catalyst is present in the above study, the light response of the undecorated P3HT:PCBM photoelectrode is clear. In the dark, the photocathode is inactive; no substantial increase in current density occurs with applied voltage. A small amount of dark current is observed (2-3 μA cm^{-2}), likely due to the moderate conductivity of the polymer film even without illumination or some unaccounted for electrochemical transfer. When the same sample is placed under 1 sun AM 1.5 irradiation, a significant boost in photocurrent is observed. Notably, the current response appears to begin before the (H^+/H_2) redox potential because a photovoltage is now produced under illumination that adds with the bias applied by the potentiostat. The clear photocurrent production

demonstrates that this solitary organic photocathode is capable of light-driven H_2 evolution in acid.

The obtained V_{oc} of 414 mV in solution is slightly lower but comparable with values reported in the literature for P3HT:PCBM bulk heterojunction solar cells.[23] However, with no active HER catalyst, photocurrent density is low (-20 μA cm^{-2} at -120 mV vs. SHE), indicating a massive overpotential would be required to drive the catalysis on the surface of the organic phase by itself. Consequently, the photocurrent density limits the overall solar-to-hydrogen (STH) efficiency to 0.016%. Low photocurrent is a clear indicator that the bare BHJ is not catalytically active for HER by itself, probably due to phase immiscibility between the polymer and surrounding aqueous solution resulting in poor electrical contact. Nonetheless, these results are promising moving forward.

3.4.3 JV Characteristics of a Catalyst-sensitized Photocathode

In attempt to improve photocurrent production, our platinum nanoparticles were introduced as embedded HER catalysts on the surface of the P3HT:PCBM bulk heterojunction. The resulting catalyst-coated photoelectrode was heated at 180 ^{o}C because heat-treated catalyst had previously given the best results following surfactant removal (highest current densities at lowest overpotentials). Figure 39 shows the JV curve obtained when the new photoelectrode was evaluated under light irradiation.

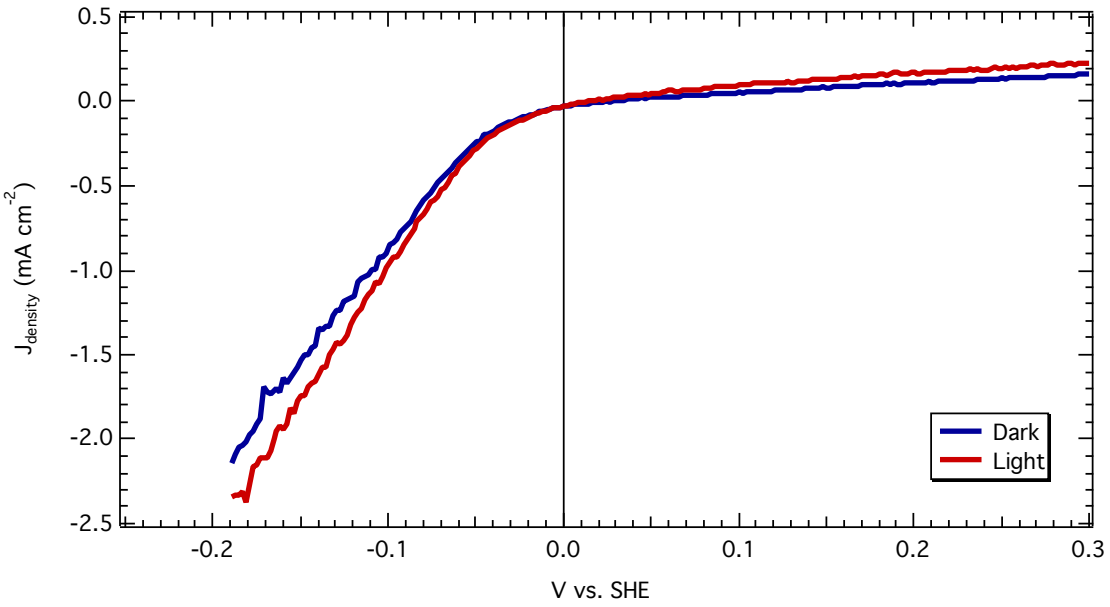

Figure 39: Light and dark light JV curves for an ITO/PEDOT:PSS/P3HT:PCBM/PtNP electrode cycled at 50 mV s^{-1} in 0.5M H_2SO_4 under 100 mW cm^{-2} illumination at AM1.5.

With the platinum catalyst present, light response is cut drastically and the electrode functions as a dark catalyst. The achieved current densities in the dark (2.08 mA cm^{-2} at -0.180 mV) and light (2.37 mA cm^{-2} at -0.180 mV) are orders of magnitude higher than those for the bare P3HT:PCBM devices but lower than the films of the pure catalyst.

It is important to note that Figure 39 is representative the best results we obtained; photoelectrodes constructed with ethanol and acetic acid washed PtNPs demonstrated lower current densities and no discernable change under dark/light conditions. This warrants investigations and further studies to better contact phases without shorting the catalyst layer to the anode. Addition of a protective n-type layer to serve as an electron transporter may protect the organic phase and better contact the platinum nanoparticles. However, PCBM should not be used (as shown by the 1:2 and bilayer electrode results,

Figure 37), as it leads to film delamination in solution. One option may be to introduce a TiO_2 layer to facilitate photoexcited electron transfer to the catalyst. The previously cited MoS_3-sensitized BHJ photoelectrode takes such an approach.[61] This report by Bourgeteau et al. does not explicitly address why the introduction of the TiO_2 interlayer affords extra device stability but the answer may lie in the energetic compatibility of the involved materials (Figure 40).

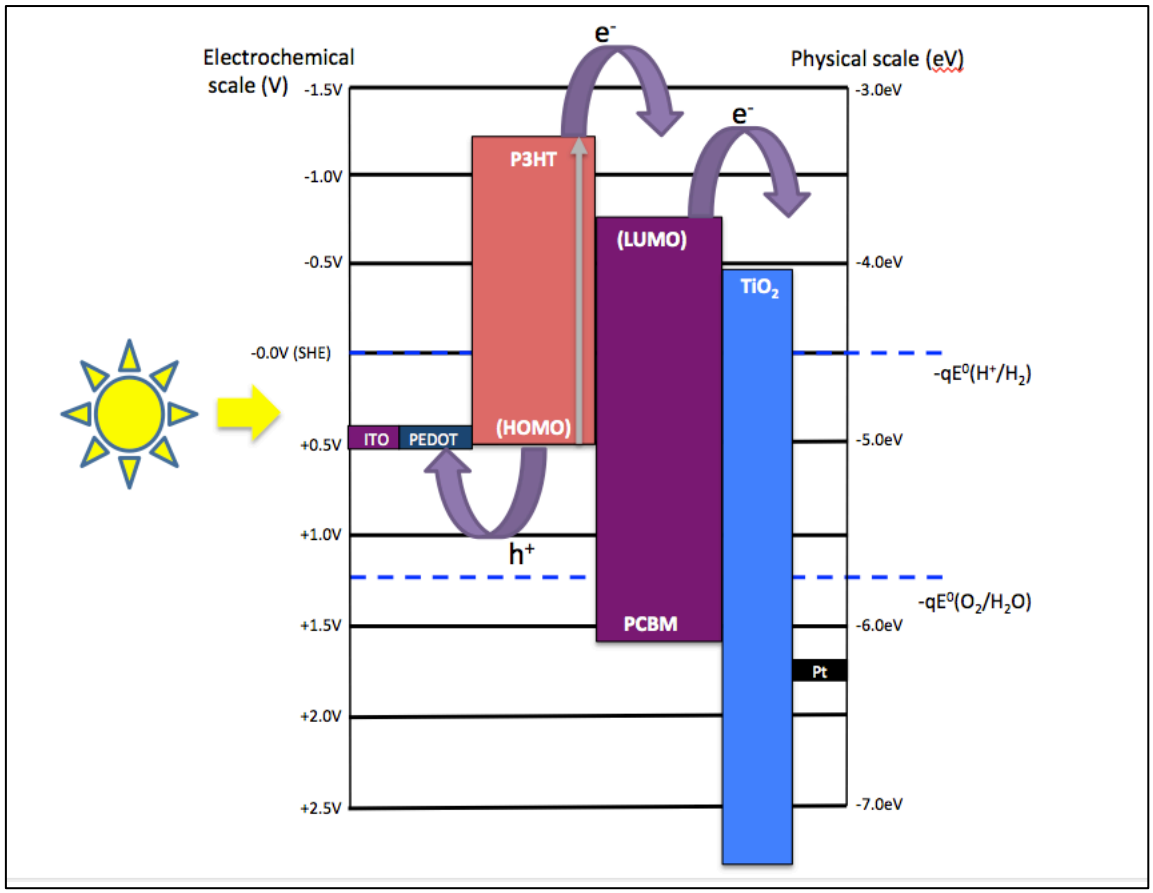

Figure 40: Schematic band energy diagram for a BHJ photoelectrode including the n-type semiconductor TiO_2.

In organic BHJ solar cells, the difference in work function of the anode and cathode produce an intrinsic electrical field that drives separation of photogenerated free

charges (electrons and holes). ITO is commonly employed as a high work function (about 5.0 eV) anode that matches well with the HOMO of P3HT, forming an ohmic contact.[64] Low work function metals like aluminum (4.1 eV) that match the LUMO of PCBM are then typically evaporated as the cathode.[65] When an external bias is applied, the Fermi levels between the two contacts (ITO and Al) align and the semiconductor bands tilt to facilitate hole transport to the anode and electron transport to the cathode. However, in a BHJ electrode, the catalyst layer is made of high work function platinum (6.35 eV [66], see Figure 40 above), which results in unfavorable energetics causing bands to bend in opposite directions. It was expected that the use of nanoscale platinum would allow some portion of the electrolyte solution to diffuse around the nanoparticle to the semiconductor phase so that the (H^+/H_2) redox potential in solution could act as a low work function metal contact. Unfortunately, our results show this does not occur. From our tests, even deposition of high catalyst loads yielding many layers are still considerably porous (Figure 22, Table 1). Even with thin catalyst coverage, the extremely nonpolar polymer layer does not make good electrical contact with the aqueous solution. By introducing an inorganic TiO_2 interlayer between the organic and catalyst phase, the band energetics should once again favor flow of electrons towards solution (Figure 40). Even a thin layer of TiO_2 could provide ample driving force for charge separation and allow higher mass loads of catalyst to be used.

CHAPTER 4: CONCLUSIONS

High surface area platinum nanoparticles (3-5 nm) were synthesized and evaluated for catalytic hydrogen evolution. Compared to the bulk metal, our PtNPs clearly demonstrate superior catalytic current densities at the same applied overpotential, likely due to the huge increase in catalyst surface area. At modest catalyst loadings, fabricated ITO/PtNPs electrodes are stable on the timescale of our experiments although precautions must be taken to remove the buildup of reaction products (H_2 bubbles) and keep the electrode surface free. When the PtNP mass load is increased, the current generation also improves. However, at extremely high catalyst loadings, performance drops as a result of a smaller electrochemically active surface area. Ligand coverage on the PtNPs directly blocks surface reaction sites and prevents direct contact between particles. HER activity improved following removal of bound surfactants and electrocatalytic ability was observed to be strongly dependent on the removal method. Thermal processing was the most successful technique, followed by multiple wash cycles in ethanol and stirring for long periods of time in acetic acid. After being subjected to 200 ^{o}C for 30 minutes, the Tafel slope decreased from 74.1 ± 1.0 mV dec^{-1} for the untreated PtNPs to 41.5 ± 1.1 mV dec^{-1}. Hydrogen evolution was therefore found to proceed by a Volmer-Heyrovsky reaction mechanism on the heated platinum nanoparticle surface. A small Tafel slope indicates a better catalyst since small overpotential increases effectively produce large changes in current density. For our three separate ligand removal methods (heat treatment, EtOH wash, HOAc stir), the calculated exchange current densities were

comparable to smooth platinum (-3.1 log [A cm^{-2}]), which shows the activation energy of hydrogen adsorption is similar to the bulk metal.

A organic photocathode was created based on the well studied P3HT:PCBM bulk heterojunction. The optimal blend ratio was 1:1 and active layers had to be sufficiently thick (approximately 260 nm) to prevent solution from penetrating to the water-soluble PEDOT:PSS hole extraction layer and delaminating the film. Fabricated electrodes demonstrated a sensitive and consistent response to visible light and were evaluated for solar hydrogen generation. In solution, the bare BHJ achieved a max V_{oc} of 414 mV and short circuit current density of 0.013 mA cm^{-2}. The V_{oc} is comparable to typical literature values for P3HT:PCBM solar cells but the J_{sc} is extremely low, arising from poor electrical contact between the organic polymer and surrounding aqueous solution. As a consequence, the small photocurrent ultimately limits device efficiency. Calculated solar-to-hydrogen efficiency for the bare P3HT:PCBM bulk heterojunction photoelectrode was 0.016%. The P3HT polymer was found to not readily degrade in solution, although PCBM may pose an issue, as blends with high PCBM ratios tend to dissociate after submersion.

Unfortunately, When the PtNP electrocatalysts were introduced to the P3HT:PCBM photoelectrode, light responsiveness was severely impeded and the device appeared to function as a dark catalyst with almost no difference between light/dark cycles. Current densities were several orders of magnitude higher due to the presence of platinum catalyst (2.37 mA cm^{-2} at -0.180 V vs. SHE) but still much lower than ITO/catalyst devices (approximately 120 mA cm^{-2} at -0180 V vs. SHE). In future work, this may be addressed by introducing another n-type semiconductor layer to facilitate

electron transport between the photoactive phase and the surface catalyst. However, PCBM should not be used due to its previously mentioned stability issues in acidic media. The use of a TiO_2 layer as an alternative has been reported in the literature and may offer a solution due to favorable band energetics.

It is our belief that this work will be advantageous to the development of new organic PECs based on the direct sensitization of current organic solar cells with heterogeneous electrocatalysts. Currently, platinum is still among the most active HER catalysts. Further efforts may include the use of modified Pt core-shell nanospheres or other nanostructured architectures that limit platinum consumption. Eventually, our optimized photocathode may be combined with a suitable photoanode bearing an appropriate OER catalyst that can simultaneously drive water oxidation. This represents the ultimate goal: an efficient system that embraces the benefits (cheapness, solution processability, flexibility) of modern organic solar cells to drive water photoelectrolysis and produce clean hydrogen fuel.

REFERENCES

(1) *Int. Energy Agency* **2014**, 6,24,28.

(2) Tsao, J.; Lewis, N.; Crabtree, G. *Solar FAQs*; 2006.

(3) Dam, H. F.; Larsen-Olsen, T. T. How do polymer solar cells work http://plasticphotovoltaics.com/lc/lc-polymersolarcells/lc-how.html.

(4) Ginley, D.; Green, M. A.; Collins, R. *MRS Bull.* **2011**, *33*, 355–364.

(5) Green, M. A.; Emery, K.; Hishikawa, Y.; Warta, W.; Dunlop, E. D. *Prog. Photovoltaics Res. Appl.* **2012**, *20*, 12–20.

(6) Desert, C. of the. Hydrogen Properties, 2001.

(7) Wallner, T.; Lohsebusch, H.; Gurski, S.; Duoba, M.; Thiel, W.; Martin, D.; Korn, T. *Int. J. Hydrogen Energy* **2008**, *33*, 7607–7618.

(8) Maniaci, D. *45th AIAA Aerosp. Sci. Meet. Exhib.* **2007**.

(9) Suleman, F.; Dincer, I.; Agelin-Chaab, M. *Int. J. Hydrogen Energy* **2015**, *40*, 6976–6987.

(10) Balat, M. *Int. J. Hydrogen Energy* **2008**, *33*, 4013–4029.

(11) Kudo, A.; Miseki, Y. *Chem. Soc. Rev.* **2009**, *38*, 253–278.

(12) Gust, D.; Moore, T. A.; Moore, A. L. *Acc. Chem. Res.* **2009**, *42*, 1890–1898.

(13) Walter, M. G.; Warren, E. L.; McKone, J. R.; Boettcher, S. W.; Mi, Q. X.; Santori, E. A.; Lewis, N. S. *Chem. Rev.* **2011**, *111*, 5815.

(14) Fujishima, A.; Honda, K. *Nature* **1972**, *238*, 37–38.

(15) Schilinsky, P.; Waldauf, C.; Brabec, C. J. *Appl. Phys. Lett.* **2002**, *81*, 3885.

(16) Padinger, F.; Rittberger, R. S.; Sariciftci, N. S. *Adv. Funct. Mater.* **2003**, *13*, 85–88.

(17) Reyes-Reyes, M.; Kim, K.; Carroll, D. L. *Appl. Phys. Lett.* **2005**, *87*, 083506.

(18) Ma, W.; Yang, C.; Gong, X.; Lee, K.; Heeger, A. J. *Adv. Funct. Mater.* **2005**, *15*, 1617–1622.

(19) Dang, M. T.; Hirsch, L.; Wantz, G. *Adv. Mater.* **2011**, *23*, 3597–3602.

(20) Švrček, V. *Pure Appl. Chem.* **2010**, *82*.

(21) Yu, G.; Gao, J.; Hummelen, J. C.; Wudl, F.; Heeger, A. J. *Science (80-.).* **1995**, *270*, 1789–1791.

(22) Björström, C. M.; Bernasik, A.; Rysz, J.; Budkowski, A.; Nilsson, S.; Svensson, M.; Andersson, M. R.; Magnusson, K. O.; Moons, E. *J. Phys. Condens. Matter* **2005**, *17*, L529–L534.

(23) Scharber, M. C.; Mühlbacher, D.; Koppe, M.; Denk, P.; Waldauf, C.; Heeger, A. J.; Brabec, C. J. *Adv. Mater.* **2006**, *18*, 789–794.

(24) Xu, Z.; Chen, L.-M.; Chen, M.-H.; Li, G.; Yang, Y. *Appl. Phys. Lett.* **2009**, *95*, 013301.

(25) Deibel, C.; Dyakonov, V. *Reports Prog. Phys.* **2010**, *73*, 096401.

(26) Hoppe, H.; Sariciftci, N. S.; Meissner, D. *Mol. Cryst. Liq. Cryst.* **2010**.

(27) Moulé, A. J.; Bonekamp, J. B.; Meerholz, K. *J. Appl. Phys.* **2006**, *100*, 094503.

(28) Wang, D. H.; Kim, J. K.; Park, O. O.; Park, J. H. *Energy Environ. Sci.* **2011**, *4*, 1434–1439.

(29) Kim, H.; So, W.; Moon, S. *J. KOREAN Phys. Soc.* **2006**, *48*, 441–445.

(30) Abe, T.; Tobinai, S.; Taira, N.; Chiba, J.; Itoh, T.; Nagai, K. *J. Phys. Chem. C* **2011**, *115*, 7701–7705.

(31) Lanzarini, E.; Antognazza, M. R.; Biso, M.; Ansaldo, A.; Laudato, L.; Bruno, P.; Metrangolo, P.; Resnati, G.; Ricci, D.; Lanzani, G. *J. Phys. Chem. C* **2012**, *116*, 10944–10949.

(32) Gustafson, M. P.; Clark, N.; Winther-Jensen, B.; MacFarlane, D. R. *Electrochim. Acta* **2014**, *140*, 309–313.

(33) Rothenberg, G. *Catalysis: Concepts and Green Applications*; Wiley-VCH Verlag GmbH & Co. KGaA: Weinheim, Germany, 2008.

(34) Trasatti, S. *J. Electroanal. Chem. Interfacial Electrochem.* **1972**, *39*, 163–184.

(35) McKone, J. R.; Warren, E. L.; Bierman, M. J.; Boettcher, S. W.; Brunschwig, B. S.; Lewis, N. S.; Gray, H. B. *Energy & Environmental Science*, 2011, *4*, 3573.

(36) Popczun, E. J.; Read, C. G.; Roske, C. W.; Lewis, N. S.; Schaak, R. E. *Angew. Chemie - Int. Ed.* **2014**, *53*, 5427–5430.

(37) Li, Y.; Wang, H.; Xie, L.; Liang, Y.; Hong, G.; Dai, H. *J. Am. Chem. Soc.* **2011**, *133*, 7296–7299.

(38) Miles, M. H. *J. Electroanal. Chem. Interfacial Electrochem.* **1975**, *60*, 89–96.

(39) Conway, B. E.; Tilak, B. V. *Electrochim. Acta* **2002**, *47*, 3571–3594.

(40) Zhang, T.; Anderson, A. B. *J. Phys. Chem. C* **2007**, *111*, 8644–8648.

(41) Conway, B. E.; Tilak, B. V. *Adv. Catal.* **1992**, *38*, 1–147.

(42) Liao, L.; Zhu, J.; Bian, X.; Zhu, L.; Scanlon, M. D.; Girault, H. H.; Liu, B. *Adv. Funct. Mater.* **2013**, *23*, 5326–5333.

(43) Chang, M.-Y.; Chen, Y.-F.; Tsai, Y.-S.; Chi, K.-M. *J. Electrochem. Soc.* **2009**, *156*, B234.

(44) Yu, Y.-Y.; Chan, S.-H. *Thin Solid Films* **2013**, *544*, 175–181.

(45) Bard, A. J.; Whitesides, G. M.; Zare, R. N.; McLafferty, F. W. *Acc. Chem. Res.* **1995**, *28*, 91–91.

(46) Bak, T.; Nowotny, J.; Rekas, M.; Sorrell, C. . *Int. J. Hydrogen Energy* **2002**, *27*, 991–1022.

(47) Ni, M.; Leung, M. K. H.; Leung, D. Y. C.; Sumathy, K. *Renew. Sustain. Energy Rev.* **2007**, *11*, 401–425.

(48) Sun, S. H.; Murray, C. B.; Weller, D.; Folks, L.; Moser, A. *Science (80-.).* **2000**, *287*, 1989–1992.

(49) Li, D.; Wang, C.; Tripkovic, D.; Sun, S.; Markovic, N. M.; Stamenkovic, V. R. *ACS Catal.* **2012**, *2*, 1358–1362.

(50) Perez, H.; Pradeau, J.-P.; Albouy, P.-A.; Perez-Omil, J. *Chem. Mater.* **1999**, *11*, 3460–3463.

(51) Kamat, P. V. *J. Phys. Chem. B* **2002**, *106*, 7729–7744.

(52) Xing, Y. *J. Phys. Chem. B* **2004**, *108*, 19255–19259.

(53) Rioux, R. M.; Song, H.; Hoefelmeyer, J. D.; Yang, P.; Somorjai, G. A. *J. Phys. Chem. B* **2005**, *109*, 2192–2202.

(54) Song, Y.; Garcia, R. M.; Dorin, R. M.; Wang, H.; Qiu, Y.; Coker, E. N.; Steen, W. A.; Miller, J. E.; Shelnutt, J. A. *Nano Lett.* **2007**, *7*, 3650–3655.

(55) Chung, D. Y.; Chung, Y. H.; Jung, N.; Choi, K. H.; Sung, Y. E. *Phys. Chem. Chem. Phys.* **2013**, *15*, 13658–13663.

(56) Bockris, J. O.; Azzam, A. M. *Trans. Faraday Soc.* **1952**, *48*, 145.

(57) Sawyer, D. T.; Sobkowiak, A.; Roberts, J. L. *Electrochemistry for Chemists*; John Wiley, NY, 1995.

(58) Thomas, J. G. N. *Trans. Faraday Soc.* **1961**, *57*, 1603.

(59) Xu, Z.; Shen, C.; Hou, Y.; Gao, H.; Sun, S. *Chem. Mater.* **2009**, *21*, 1778–1780.

(60) El-Rashiedy, O. A.; Holdcroft, S. *J. Phys. Chem.* **1996**, *100*, 5481–5484.

(61) Bourgeteau, T.; Tondelier, D.; Geffroy, B.; Brisse, R.; Laberty-Robert, C.; Campidelli, S.; de Bettignies, R.; Artero, V.; Palacin, S.; Jousselme, B. *Energy. Sustain. Soc.* **2013**, *6*, 2706–2713.

(62) Zimmermann, B.; Würfel, U.; Niggemann, M. *Sol. Energy Mater. Sol. Cells* **2009**, *93*, 491–496.

(63) Manceau, M.; Rivaton, A.; Gardette, J.-L.; Guillerez, S.; Lemaître, N. *Polym. Degrad. Stab.* **2009**, *94*, 898–907.

(64) Schlaf, R.; Murata, H.; Kafafi, Z. . *J. Electron Spectros. Relat. Phenomena* **2001**, *120*, 149–154.

(65) Huber, E. E.; Kirk, C. T. *Surf. Sci.* **1966**, *5*, 447–465.

(66) Kötz, E. R.; Neff, H.; Müller, K. *J. Electroanal. Chem. Interfacial Electrochem.* **1986**, *215*, 331–344.